https://ntrs.nasa.gov/search.jsp?R=20110013473 2019-08-30T16:18:57+00:00Z

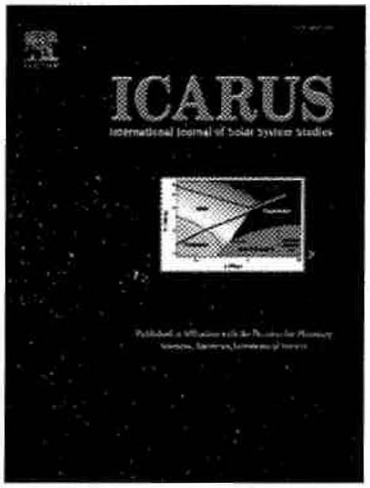

Long-term evolution of the aerosol debris cloud produced by the 2009 impact on jupiter

A. Sánchez-Lavega, G.S. Orton, R. Hueso, S. Pérez-Hoyos, L.N. Fletcher, E. García-Melendo, J.M. Gomez-Forrellad, I. de Pater, M. Wong, H.B. Hammel, P. Yanamandra-Fisher, A. Simon-Miller, N. Barrado-Izagirre, F. Marchis, O. Mousis, J.L. Ortiz, J. García-Rojas, M. Cecconi, J.T. Clarke, K. Noll, S. Pedraz, A. Wesley, P. Kalas, N. McConnell, W. Golisch, D. Griep, P. Sears, E. Volquardsen, V. Reddy, M. Shara, R. Binzel, W. Grundy, J. Emery, A. Rivkin, C. Thomas, D. Trilling, K. Bjorkman, A.J. Burgasser, H. Campins, T.M. Sato, Y. Kasaba, J. Ziffer, R. Mirzoyan, M. Fitzgerald, H. Bouy

PII: S0019-1035(11)00099-6
DOI: 10.1016/j.icarus.2011.03.015
Reference: YICAR 9758

To appear in: *Icarus*

Received Date: 27 September 2010
Revised Date: 3 March 2011
Accepted Date: 3 March 2011

Please cite this article as: Sánchez-Lavega, A., Orton, G.S., Hueso, R., Pérez-Hoyos, S., Fletcher, L.N., García-Melendo, E., Gomez-Forrellad, J.M., de Pater, I., Wong, M., Hammel, H.B., Yanamandra-Fisher, P., Simon-Miller, A., Barrado-Izagirre, N., Marchis, F., Mousis, O., Ortiz, J.L., García-Rojas, J., Cecconi, M., Clarke, J.T., Noll, K., Pedraz, S., Wesley, A., Kalas, P., McConnell, N., Golisch, W., Griep, D., Sears, P., Volquardsen, E., Reddy, V., Shara, M., Binzel, R., Grundy, W., Emery, J., Rivkin, A., Thomas, C., Trilling, D., Bjorkman, K., Burgasser, A.J., Campins, H., Sato, T.M., Kasaba, Y., Ziffer, J., Mirzoyan, R., Fitzgerald, M., Bouy, H., Long-term evolution of the aerosol debris cloud produced by the 2009 impact on jupiter, *Icarus* (2011), doi: 10.1016/j.icarus.2011.03.015

This is a PDF file of an unedited manuscript that has been accepted for publication. As a service to our customers we are providing this early version of the manuscript. The manuscript will undergo copyediting, typesetting, and review of the resulting proof before it is published in its final form. Please note that during the production process errors may be discovered which could affect the content, and all legal disclaimers that apply to the journal pertain.

LONG-TERM EVOLUTION OF THE AEROSOL DEBRIS CLOUD PRODUCED BY THE 2009 IMPACT ON JUPITER

A. Sánchez-Lavega[1], G. S. Orton[2,34], R. Hueso[1], S. Pérez-Hoyos[1], L. N. Fletcher[3,34], E. García-Melendo[4], J. M. Gomez-Forrellad[4], I. de Pater[5], M. Wong[5], H. B. Hammel[6], P. Yanamandra-Fisher[2], A. Simon-Miller[7], N. Barrado-Izagirre[8], F. Marchis[5,9], O. Mousis[10], J. L. Ortiz[11], J. García-Rojas[12], M. Cecconi[13], J. T. Clarke[14], K. Noll[15,33], S. Pedraz[16], A. Wesley[17], P. Kalas[5], N. McConnell[5], W. Golisch[18], D. Griep[18], P. Sears[18], E. Volquardsen[18], V. Reddy[19,34], M. Shara[20,34], R. Binzel[21,34], W. Grundy[22,34], J. Emery[23,34], A. Rivkin[24,34], C. Thomas[25,34], D. Trilling[25,34], K. Bjorkman[26,34], A. J. Burgasser[27,34], H. Campins[28,34], T. M. Sato[29,34], Y. Kasaba[29,34], J. Ziffer[30,34], R. Mirzoyan[31], M. Fitzgerald[32], H. Bouy[33] and the International Outer Planet Watch Team (IOPW-PVOL)[35].

1. Departamento de Física Aplicada I, Escuela T. Superior de Ingeniería, Universidad del País Vasco, Bilbao, Spain.
2. MS 169-237, Jet Propulsion Laboratory, California Institute of Technology, 4800 Oak Grove Dr., Pasadena, CA, 91109, USA.
3. Atmospheric, Oceanic & Planetary Physics, Department of Physics University of Oxford, Clarendon Laboratory, Parks Road, Oxford, OX1 3PU, UK.
4. Fundació Privada Observatori Esteve Duran, Montseny 46, 08553 Seva, Spain.
5. Astronomy Department, 601 Campbell Hall, University of California, Berkeley, CA 94720, USA.
6. Space Science Institute, 4750 Walnut Avenue, Suite 205, Boulder, CO 80301, USA.
7. NASA Goddard Space Flight Center Greenbelt, MD 20771, USA.
8. Departamento de Matemática Aplicada, E.U.I.T.I., Universidad del País Vasco, Bilbao, Spain.
9. Carl Sagan Center at the SETI Institute, 189 Bernardo Av., Mountain View, CA 94043, USA.
10. Observatoire de Besançon, Institut UTINAM, UMR/CNRS 6213, 41 bis Avenue de l'Observatoire, BP 1615, 25010 Besançon Cedex, France.
11. Instituto de Astrofísica de Andalucía, C.S.I.C., Granada, Spain.
12. Instituto de Astrofísica de Canarias, La Laguna (Tenerife), Spain & Departamento de Astrofísica, Universidad de La Laguna. E-38205 La Laguna, Tenerife, Spain
13. Fundación Galileo Galilei – INAF, Rambla José Ana Férnandez Pérez, 7 38712 San Antonio de Breña Baja, La Palma, Spain.
14. Center for Space Physics, Boston University, 957 Commonwealth Ave., Boston, MA 02215, USA.
15. Space Science Institute, 72 Sarah Bishop Rd., Ridgefield, CT 06877, USA.
16. Calar Alto Obs Centro Astronómico Hispano Alemán, Calle Jesús Durbán Remón 2-2, 04004 Almeria, Spain
17. Acquerra Pty. Ltd., 82 Merryville Drive, Murrumbateman NSW, Australia.
18. Institute for Astronomy, University of Hawaii, 640 N. Aohoku Pl., Hilo, HI 96720, USA
19. Dept. of Space Studies, Clifford Hall, Univ. N. Dakota, Room 520, 4949 University Ave. Stop 9008, Grand Forks, ND 58202-9008, USA
20. Astrophysics Dept., American Museum of Natural History, Central Park West & 79th St., New York, NY 10024-5192, USA
21. MS 54-410, Dept. of Earth & Planetary Sci., Massachusetts Institute of Technology, 77 Massachusetts Ave., Cambridge, MA 02139-4301, USA

22. Lowell Observatory, 1400 W. Mars Hill Rd., Flagstaff, AZ 86001, USA
23. 306 Earth & Planetary Sciences Bldg, 1412 Circle Dr., Univ. Tennessee, Knoxville, TN 37996-1410, USA
24. NP3-E169, Applied Physics Laboratory, Johns Hopkins University, 11100 Johns Hopkins Rd., Laurel, MD 20723, USA
25. Dept. of Physics & Astronomy, Northern Arizona University, P. O. Box 6010, Flagstaff, AZ 86011, USA
26. Dept. of Physics & Astronomy, MS #111, Univ. of Toledo, Toledo, OH 43606-3390, USA,
27. Dept. of Physics, Mail Code 0424, University of California, San Diego, 9500 Gilman Dr., La Jolla, CA 92093, USA.
28. Dept. of Physics, University of Central Florida, Orlando, FL 32816-2385, USA
29. Tohoku University, Aramaki-Aza-Aoba 6-3, Aoba-ku, Sendai, 980-8578, Japan
30. Univ. Southern Maine, 96 Falmouth Street, P. O. Box 9300, Portland, ME 04104-9300, USA.
31. Glendale Community College, 1500 N. Verdugo Rd., Glendale, CA 91208, USA.
32. Institute of Geophysics and Planetary Physics, Lawrence Livermore National Laboratory, 7000 East Ave., Livermore, CA 94550, US, and Department of Physics and Astronomy, University of California, Los Angeles, 90095-1547, USA
33. Centro de Astrobiologia (INTA-CSIC), PO BOX 78, 28691 Villanueva de la Cañada, Madrid, Spain
34. Visiting Astronomer at the Infrared Telescope Facility, which is operated by the University of Hawaii under Cooperative Agreement no. NNX-08AE38A with the National Aeronautics and Space Administration, Science Mission Directorate, Planetary Astronomy Program
35. Contributors to the IOPW-PVOL database are listed at http://www.pvol.ehu.es/

Number of pages: 41
Number of Tables: 1
Number of Figures: 13

Submitted to Icarus, 27 September 2010
Revised: 3 February 2011

Running title: Evolution of Jupiter's 2009 Impact Cloud

Corresponding author address:
Agustín Sánchez-Lavega
Departamento de Física Aplicada I
E.T.S. Ingeniería
Universidad del País Vasco
Alameda Urquijo s/n
48013 Bilbao, Spain
E-mail: agustin.sanchez@ehu.es

ABSTRACT

We present a study of the long-term evolution of the cloud of aerosols produced in the atmosphere of Jupiter by the impact of an object on 19 July 2009 [Sánchez-Lavega et al., 2010. The Impact of a Large Object on Jupiter in July 2009, *ApJL*, **715**, L155-159]. The work is based on images obtained during 5 months from the impact to 31 December 2009 taken in visible continuum wavelengths and from 20 July 2009 to 28 May 2010 taken in near-infrared deep hydrogen-methane absorption bands at 2.1-2.3 microns. The impact cloud expanded zonally from ~ 5000 km (July 19) to 225,000 km (29 October, about 180° in longitude), remaining meridionally localized within a latitude band from 53.5°S to 61.5°S planetographic latitude. During the first two months after its formation the site showed heterogeneous structure with 500–1000 km sized embedded spots. Later the reflectivity of the debris field became more homogeneous due to clump mergers. The cloud was mainly dispersed in longitude by the dominant zonal winds and their meridional shear, during the initial stages, localized motions may have been induced by thermal perturbation caused by the impact's energy deposition. The tracking of individual spots within the impact cloud shows that the westward jet at 56.5°S latitude increases its eastward velocity with altitude above the tropopause by 5-10 ms^{-1}. The corresponding vertical wind shear is low, about 1 ms^{-1} per scale height in agreement with previous thermal wind estimations. We found evidence for discrete localized meridional motions with speeds of 1-2 ms^{-1}. Two numerical models are used to simulate the observed cloud dispersion. One is a pure advection of the aerosols by the winds and their shears. The other uses the EPIC code, a nonlinear calculation of the evolution of the potential vorticity field generated by a heat pulse that simulates the impact. Both models reproduce the observed global structure of the cloud and the dominant zonal dispersion of the aerosols, but not the details of the cloud morphology. The reflectivity of the impact cloud decreased exponentially with a characteristic timescale of 15 days; we can explain this behavior with a radiative transfer model of the cloud optical depth coupled to an advection model of the cloud dispersion by the wind shears. The expected sedimentation time in the stratosphere (altitude levels 5-100 mbar) for the small aerosol particles forming the cloud is 45-200 days, thus aerosols were removed vertically over the long term following their zonal dispersion. No evidence of the cloud was detected 10 months after the impact.

1. INTRODUCTION

On July 19, 2009 an object with an estimated size of ~ 500 m collided with Jupiter generating a debris cloud (thereafter called "the impact cloud" or IC) in the upper atmosphere with an east-west length of ~4,800 km (Sánchez-Lavega et al., 2010).. The debris cloud was subsequently dispersed by the Jovian winds at the impact latitude of 58.5°S (planetographic) (Hammel et al., 2010). The initial behavior of the IC globally resembled that observed for the individual SL9 impacts in 1994 (Hammel et al., 1995; West et al., 1995; Clarke et al., 1995; Sánchez-Lavega et al., 1995; Simon and Beebe, 1996; Banfield et al., 1996). However, we found some differences between the 2009 and SL9 impacts.

For SL9, Sánchez-Lavega et al. (1998a) studied the long-term evolution of the aerosols caused by dispersion, mixing and vertical sedimentation. They found that after two years, a thin aerosol layer formed a wide band that fully covered the whole latitude circle, indicating dispersion in latitude by the action of the usually elusive meridional motions and low sedimentation rates consistent with small aerosol particles. The analysis of the dispersion of each individual element of the 1994 cloud debris (i.e. produced by each impact) was complicated by the mixing of material between adjacent impact sites. In contrast, for the 2009 event we had a single impact and the dispersion and spreading of the IC was easier to track, allowing for a better interpretation of the phenomenon. The study of the dispersion and evolution of the IC gives information on the physical state of the Jovian atmosphere allowing a direct inference of the vertical structure of the winds in the stratosphere, in particular at its upper parts where the aerosols can be used as tracers of the flow. It also gives information on the microphysical processes that took place within the cloud and led to sedimentation of the debris. Impact events such as this one and Shoemaker-Levy 9 in Jupiter allow us to compare the disperson and transport of energy and material left in the atmospheres of both planets, the induced local dynamics and aerosol microphysics (particle sedimentation, coagulation and coalescence). For the Earth, such studies are enabled by observations of cloud ashes produced during volcanic eruptions that inject aerosols in the upper troposphere and lower stratosphere (see e.g. Boville et al., 1991, Stowe et al. 1992; Trepte et al. 1993; McCormick and Veiga, 1992; Jonsson et al., 1996; Allen et al, 1999). A comparison of these processes in the Earth with Jupiter is enabled only by observations of these rare impact events.

In this paper, we concentrate on the debris cloud evolution in 2009, from its very first detection on July 19 through December 31 when the cloud was barely visible. . The work represents a large effort by an international team that gathered images of the event over a broad wavelength range with a battery of telescopes and observatories, most of them listed in previous works on the impact (Sánchez-Lavega et al., 2010; Hammel et al., 2010; de Pater et al., 2010a; Fletcher et al., 2010; Orton et al., 2011), as discussed in Section 2. We focus this study on images taken in two wavelength ranges: (1) visual range, broadly ~ 250 – 950 nm; and (2) near-infrared hydrogen and methane absorption bands (2.12 – 2.3 μm). Within each range we analyzed images taken with a variety of filters that have different bandwidths. The aerosol cloud can be well separated as a dark feature from the quiescent background atmosphere due to the high particle absorption in continuum wavelengths (Hammel et al., 2010; de Pater et al., 2010a), or as a bright feature on images taken in the gas absorption bands due to the high particle altitude. From the evolution and motions of the IC's aerosol cloud elements reported in Section

3, we derive the global wind structure in the Jovian stratosphere at the impact latitude and discuss the presence of local regional dynamics. In Section 4 we present two dynamical models to explain the aerosol cloud evolution: a pure advection of the cloud by the winds and their shears, and non-linear EPIC code simulations that served to put an upper limit to the energy deposition in Jupiter's stratosphere. Finally, from the reflectivity measurements and a radiative transfer model we calculate the aerosol optical depth evolution that is compared to that expected from the zonal dispersion and particle sedimentation.

2. OBSERVATIONS AND IMAGE ANALYSIS

The images obtained in the visual range (~ 250-950 nm) correspond to two main sets. The first set is comprised of images from July 19 to September 20 provided by a large team of contributors to the International Outer Planet Watch (IOPW) and the Planetary Virtual Observatory Laboratory PVOL data base (Hueso et al., 2010). This data set has a daily temporal coverage of the IC evolution with small telescopes. The second set was the high-resolution observations obtained by the Hubble Space Telescope (HST) Wide Field Camera 3 (WFC3) during three runs in July 23, August 3 and August 8, and September 23, previously analyzed by Hammel et al. (2010).

The IOPW data set was obtained with a variety of telescopes, typically with apertures of 0.3-0.6 m but with some observations obtained in larger telescopes with apertures of 0.81-m (IAC80, Canary Islands) and one set from the 1.0 m (Pic du Midi Observatory). At the small telescopes, fast imaging techniques (30-60 frames per second) with well-developed image processing techniques were used to improve the resolution compared to single long-exposure (seconds) frame CCD cameras used in the larger telescopes (Cidadao, 2001; Grafton, 2003). Diffraction and seeing conditions limit the resolution to a maximum of about ~ 700 km/pixel for the best cases. Most images were sent to the IOPW-PVOL data base as processed color composites made with broadband filters in the range ~ 400-650 nm, and therefore they are not calibrated in intensity (Sánchez-Lavega et al., 2010). In addition to these "continuum wavelength composite images", a small set of single images was obtained with a narrowband methane absorption filter at 890 nm. The IC is darker than surrounding clouds in the visible continuum, from the ultraviolet to the red region and in the color composites mentioned above, due to the intrinsic absorption of the IC aerosols (Sánchez-Lavega et al., 2010; Hammel et al., 2010; Orton et al., 2011; de Pater et al., 2010a). In the 890-nm images, however, the IC is bright relative to the surroundings indicative of a relatively high altitude as previously indicated. These observations are important for two reasons. First, they provide an extended temporal coverage. Second, there are some instances in which images were made by different observers on the same day, allowing us to distinguish between small or diffuse cloud details and artifacts created by the image processing. The high-resolution HST imaging was used to complement the IOPW survey and to serve as a guide for the long-term cloud tracking of the IC features. They were also used to measure the sizes of the small dark spots, as well as the edges of the zonally extended diffuse IC very accurately: the resolution was of the order of 200 km/pixel. The details of these observations are presented in Hammel et al. (2010).

The second large set we have analyzed for this paper covers the NIR spectral window from ~1 to 2.3 μm. The observations were performed by a large international collaboration involving larger telescopes around the world, as summarized in Table 1.

Further details for some of these observations were presented by Orton et al. (2011) and de Pater et al. (2010a). We selected images taken in the NIR absorption bands at 2.12 by molecular hydrogen and at 2.23-2.3 μm by methane, both sensing the IC at higher altitudes due to the limited photon penetration in these bands. They allow us to distinguish the IC from the background even more than at 890 nm, because the IC is so bright relative to the surrounding background.

All IOPW, HST and NIR images were processed and navigated using the software LAIA based on the VICAR code (Cano, 1998). The methodology employed to perform position measurements (longitude-latitude) of the features in time and extract motions from their tracking is detailed in García-Melendo et al. (2009).

[Table 1]

The NIR images were calibrated in intensity to determine the absolute reflectivity of the IC, as described in section 5. These reflectivity data were used to analyze the optical depth evolution of the IC during the observing period. Additionally we performed the tracking of individual features in the images from July 20 to September 20. After this date, although large cloud condensations were still visible, their tracking was difficult and only the east and west "edges" of the extended IC features were tracked. This was possible until October 29. Afterwards and until December 31, the IC became homogeneous and largely extended and only area reflectivity measurements were possible. In summary, the reflectivity measurements cover the whole period from July 20 to December 31, 2009. The best coverage was during the first post-impact dates, from July 20 to August 13, when most observatories contributed to the study. After this date, most images come from the IRTF-NASA team. Details on the exact dates of coverage are given in Table 1.

3. EVOLUTION OF THE CLOUD DEBRIS AND WIND MEASUREMENTS

The first image of the IC on July 19 (Sánchez-Lavega et al., 2010) and the higher-resolution HST images of July 23 (Hammel et al., 2010) showed the initial IC with two main components: a main dark streak surrounded in its westward flank by a halo or crescent that spans between planetographic latitudes -53.5° and -60° (Figure 1). Planetographic latitudes (φ_g) are used along the text. Planetographic and planetocentric (φ_c) latitudes are related by $\tan\varphi_c = (R_P / R_E)^2 \tan\varphi_g$ (Sánchez-Lavega, 2010), being the polar and equatorial radii of Jupiter R_P = 66854 km and R_E = 71492 km (Lindal et al, 1981). Afterwards, the IC expanded preferentially in the zonal direction by the dominant zonal winds. Figure 1 shows a temporal map series, based on the IOPW and HST images as observed in the visible spectral range, where the IC appears dark and increasing in size between July 19 and September 20. Figure 2 shows the temporal map series of the IC between July 20 and October 29 as observed in the near infrared 2.12-2.3 absorption bands (NIR, Near Infrared) where the IC appears bright. The same general morphology of the IC is observed in the images taken in the 890-nm methane absorption band. A simple comparison immediately shows that the same features are observed within the IC in the continuum and methane bands but with reversed brightness. The identical cloud patterns within the IC observed at these wavelengths suggest either (a) both visible and near-IR wavelengths sense the same altitudes; or (b) the debris material is distributed uniformly over a range of altitudes (de Pater et a. 2010a). In this paper we assume that we detect the IC at the same altitude levels in the visible and near-IR. Since the debris is detected in the 2.3μm absorption bands, the IC must be located at and above the tropopause (Hammel et al., 2010; de Pater et al., 2010a). Thus the differences in darkness (absorption in the visible continuum) or brightness (reflectivity within the methane absorption bands) within the IC mostly indicate differences in optical thickness, but not large altitude differences.

[Figure 1]

[Figure 2]

Just as in the observations of the SL9 impact in 1994, the clouds spread preferentially in the zonal direction i.e. that of the prevailing winds, indicating that the aerosol transport by the zonal winds dominates the evolution of the IC morphology. However, the cloud is not homogeneous in its reflectivity (i.e. in its optical thickness) but shows a distinct distribution of clumps or spots with higher aerosol density, particularly evident during the first month after the impact. These spots were used as tracers of the motions, measuring their longitude and latitude versus time. But importantly, as the debris cloud was dispersed by the winds, it also showed an intrinsic evolution with new spot formation and in other cases with some of the spots dividing into two or more elements (Figures 1 and 2). This aspect will be discussed in section 3.3.

3.1 Longitude tracking

The evolution of the IC was determined by direct latitude and longitude measurements of the features on the navigated images and on cylindrical map projections. The tracking of the condensation spots was performed by visual identification of the same feature on successive images. We separate the tracking into three main sets, two corresponding to the zonal drift of the features and one to their meridional motion. To determine the zonal drift rate, we used two methods. In the first method, we measured the East and West longitude limits (the "edges") of the IC in the two wavelength ranges (visible and NIR) as a function of time. This is shown in Figure 3. The IOPW-HST tracking data cover the period July 19 – Aug. 14 and the NIR tracking data cover the period July 20 – Oct. 29, 2009. Afterwards, only brightness studies were performed until December 31, 2009, after that time the planet was difficult to observe due to its proximity to the Sun (solar conjunction took place on February 28.). The expansion rate of the IC edges can be reasonably fitted by a linear function $L(III) = \omega \Delta t + L_0$ with $L(III)$ the System III longitude, ω the zonal angular velocity (deg/day) and Δt = J.D. – 2450000 is the reduced Julian Date, where J.D. = 2455032 for July 19 (at 12 U.T.):

Eastern ("leading") edge: $L(III) = 0.51 \bullet \Delta t - 2259$ (1)

Western ("trailing") edge: $L(III) = -1.02 \bullet \Delta t + 5431$ (2)

According to these edge displacements, the prediction is that the east and west edges of the IC, which moved in opposite directions, should have encountered one another at longitude ~ 67° and on $\Delta t \sim 5258$ that corresponds to early March, i.e. during the solar conjunction. After solar conjunction, similar NIR observations were made in May, 2009, but by then the reflectivity at the IC latitude was indistinguishable from that of the pre-impact atmosphere.

The averaged zonal velocity, <*u*>, as retrieved from these linear fits have low errors $\sigma(<u>) \sim \Delta x / \Delta t$ that for positioning precision $\Delta x \leq 1000$ km and tracking time $\Delta t \sim$ 60-100 days give $\sigma(<u>) \sim$ 0.5-1 ms^{-1}.

[Figure 3]

In the second method, we tracked the longitude-latitude positions of individual spots within IC in the visible continuum (July 19 – Sept. 20) and in the near infrared (July 20 – October 29). The longitude drift charts of the individual tracked features are shown in Figure 4 for the visible and in Figure 5 for the near infrared. Each tracer was typically measured at least in 5 different images at different times. The minimum time interval to follow a tracer is 3 days and we found that a single tracer does not usually survive more than about 15 days, or else can not be identified as the same feature. In total, we tracked 53 spots. For completeness, we added to the tracking chart those points previously reported from our HST measurements (Hammel et al., 2010). It must be noted that some tracers were measured simultaneously in the IOPW, HST and NIR, but usually spanning different time intervals, making the results consistent. The longitude drift of each feature was fitted to a linear function obtaining the zonal angular velocity of the feature in System III and the zonal velocity (u_i). As before we expect from the tracking zonal velocity errors for each individual feature $\sigma(u_i) \leq 1 - 3.5$ ms^{-1} (positioning precision $\Delta x \leq 1000$ km and typical tracking times $\Delta t \geq$ 3 - 15 days).

[Figure 4]

[Figure 5]

3.2 Latitude tracking

Although the spreading of the IC occurred mainly in the zonal direction due to the dominant zonal winds and its meridional shear, a meridional expansion for some features was also detected. Measurements of the HST images on August 3 and 8 showed that whereas the northern limit of the IC remained at the initial latitude of -53.5°±0.5°, the southern limit was at latitude -61.4°±0.5°, i.e. closer to the pole than initially observed. This indicates that a poleward drift of the IC occurred during the first 2-3 weeks at an approximate rate of -0.1°/day. Our long-term measurements of the meridional limits of the IC (July 19 – December 30) indicates that the IC aerosols remained confined between these two latitudes -53° and -61° where two eastward jets have their peak speeds and where the gradient of the potential vorticity becomes large (see sections 3.3 and 4.3).

However, we detected a faster meridional motion, both in the visible and NIR images, for a single spot that formed in the first days after the impact (Figure 6). Tracking its motion (longitude and latitude) from July 23 to August 5 revealed that it translated from latitude -56.0° to -53.5°. Navigation errors in the high resolution HST and NIR images translate in latitude uncertainty measurements of 0.2°. The total meridional displacement of the feature was ~ 2.5° (equivalent to 3120 km) between July 23 to 30, equivalent approximately to a meridional drift rate of +0.3°/day. In summary, IC aerosols were observed to drift both poleward and equatorward, specifically during the early stages of the IC evolution.

[Figure 6]

3.3 Wind measurements

The measured longitudinal drift of each individual cloud element was transformed to the zonal wind speed at its mean latitude. In Figure 7 we present the zonal wind profile that we derived for all the features we measured within the IC and compare it with one measured using regular Jovian features using HST images obtained two years before the impact in 2007 and in the same HST images in 2009 used to track the IC features but this time using discrete features outside it. A parabolic fit to the IC velocity points is shown in Figure 7 (right) to serve as comparison with the background HST profile and to have an idea of the velocity dispersion of the IC elements. Two results emerge from these profiles. First, it is evident that the wind velocities of the IC elements are higher than those of the reference background wind profile. Since the aerosol debris is placed at a higher altitude than the background cloud (Hammel et al., 2010; de Pater et al., 2010a), these measurements indicate that the winds increase with altitude within the latitude band where the impact aerosols formed (latitudes -53° to -61°). The speed increase is within 5 to 10 ms^{-1} (which is above our estimated measurement errors). According to Hammel et al. (2010), de Pater et al. (2010a) and Orton et al. (2011), the cloud debris extended vertically from 1-20 mbar to 200-300 mbar (about 4-5 scale heights H; 1 H = 22 km). Assuming that the background wind profile is determined from cloud tracking at the 500-mbar pressure level, the vertical shear of the zonal wind is expected to be of the order of +1 ms^{-1} per scale height which is in agreement with the thermal wind speeds derived from Voyager-IRIS and Cassini-CIRS measurements at these latitudes (Simon-Miller et al., 2006).

[Figure 7]

Second, all the tracking points show a significant velocity dispersion at a given latitude with values varying by up to 10-15 ms^{-1} (e.g. at latitude -56°, Figure 7). This dispersion is well above the time-averaged velocity measurement error, which we estimated before to be $\sigma(u_i) \leq 1-3.5$ ms^{-1} from the large temporal tracking of each feature. Since we estimate the averaged error in the latitudinal position of each feature to be ± 0.5°, this indicates that although the features followed the mean atmospheric flow as nearly passive tracers of the zonal winds, they also showed intrinsic local motions. In particular, there was evidence of clump formation (condensation spots) within the IC during its expansion with clump size of order 500 – 1000 km (Figure 8). Similar clump formations and fast initial motions were observed in some of the ICs generated by the SL9 impacts (Sánchez-Lavega et al., 1995; Simon et al., 1996). The possible nature of this clump formation and their motions within the IC will be discussed below. We also note that this velocity dispersion is similar in magnitude to the fluctuations in zonal speeds as measured on timescales ranging from a Jovian rotation up to weeks or months (Asay-Davis et al. 2011).

Finally the latitudinal drifts of some features that were measured during the first two weeks after the impact were converted to meridional wind velocities. At latitude -60° the motion was poleward with a velocity of 0.8 ms^{-1} whereas in the middle of the IC at -55° the motion was equatorward with a velocity of 2 ms^{-1}. As indicated above, no further meridional spread was seen, and the IC remained confined between latitudes -53.5°±0.5° and -61.4°±0.5° until the last observation in which it was detectable.

[Figure 8]

3.4 Reflectivity measurements in the NIR absorption band

In order to study the aerosol content evolution within the IC, we performed a long-term measurement of its brightness reflectivity *I/F* in the NIR methane absorption band at 2.2 – 2.3 μm. We used for this study the images coming from the NIR dataset which corresponds to the contributing observatories numbered (3) to (9) in the first column of Table 1. According to methane band coefficients derived by Karkoschka and Tomasko (2010), the optical depth for the gas absorption at these wavelengths is unity at pressure levels ~ 1-10 mbar; thus, we are sensing the top of the IC. The reflectivity was measured relative to that of close latitudes, not affected by the impact, to account for the geometric variability across the Jovian disk, most importantly the center to limb variation. An absolute reflectivity calibration was performed by reference to the reflectivity curves in de Pater et al. (2010a). Since the cloud brightness structure was not spatially homogeneous, in particular during the first two months (Figure 2), an averaged IC reflectivity was obtained for each date from measurements across different points of the IC between July 19 and September 20. For most of the data points, the geometrical configuration corresponds to the cosine of the incident and emission angles with values $\mu \sim \mu_0 \sim 0.6$ (corresponding to the central meridian at about -58° latitude). In

Figure 9 we show the measured data point reflectivity for the IC as a function of time in this methane band together with a simple decaying exponential fit

$$\frac{I}{F}(t) = 0.0025 + \left[0.017 \quad \exp\left(-\frac{(\Delta t - 5040)}{t_D} \right) \right] \qquad (3)$$

where Δt is the reduced Julian date (Julian Date – 2,450,000; Julian Date of 19 July 2009 12:00 UT = 2,455,032) and t_D is the e-folding timescale for the reflectivity decay which we found to be ~ 15 days from the fit.

[Figure 9]

4. ANALYSIS OF THE DEBRIS CLOUD EVOLUTION

In order to interpret the structure and evolution of the IC we must first review the known dynamics of this Jupiter region. As shown in Figure 7, the impact occurred in a band where the flow is weakly westward, bounded on the north and south by two eastward jets with peak speed of ~ 30 ms^{-1} at latitude -61° and ~ 45 ms^{-1} at latitude -52° (García-Melendo and Sánchez-Lavega, 2001). The southern polar region is characterized by the presence of planetary scale waves that manifest in the morphology of the high altitude hazes and cloud field as a wavy pattern that encloses the polar region (Sánchez-Lavega et al., 1998b; Vincent et al., 2000; Barrado-Izagirre et al., 2009). There are different waves whose latitudinal location depends on the observing wavelength. The contrast is largest in the ultraviolet where they appear dark due to haze absorption. They are bright in the methane absorption bands (890 nm, 2.23 – 2.3 μm) where they vary in brightness, following a trend similar to that of the IC. Sánchez-Lavega et al. (1998b) and Barrado-Izagirre et al. (2009) demonstrated that the observed dynamics is consistent with Rossby wave activity, based on their motion and dispersion relationship. These waves serve as a diagnostic tool to test the atmospheric response to the impact at nearby latitudes.

Figure 10 is a series of map projections of the southern polar region at these wavelengths showing the IC and the south polar waves. The impact occurred midway in latitude between two waves: the poleward main wave that is prominent in the methane band images centered at latitude -65°, and an equatorward wave that is similarly prominent in the ultraviolet and is centered at -48°. These waves are prominent in the HST UV images at wavelengths 225 – 378 nm (Hammel et al., 2010) and subtly detected in thermal-IR imaging of stratospheric CH4 emission near 7.9 μm by VLT (Fletcher et al., 2010). Comparing the amplitudes and structure of these two waves in the HST images obtained in July 23, August 3 and 8, it seems that they were not affected at all by the impact. The wavy pattern was always present at the impact longitudes, without apparent significant changes in the meridional amplitude and zonal wavelength, indicating that the impact did not affect the dynamics of these permanent waves. The response of the atmosphere to the impact was restricted in latitude to the impacted band that had a meridional width of ~ 8°.

[Figure 10]

4.1 Global dispersion of the cloud debris by the zonal winds

The observed dominant zonal spread of the IC and the exponential decay of its 2.23-2.3μm reflectivity were originated by the aerosol dispersion and subsequent decrease in the particle number density and optical depth as a result of various processes. The most obvious is the dispersion produced by the prevailing zonal winds and its shear (meridional and vertical). The typical temporal scale for the aerosol dispersion due to the zonal wind shears is $t_D \approx (\partial u / \partial y)^{-1}, (\partial u / \partial z)^{-1} \sim 1\text{-}5$ days, according to the measurements reported in section 3.3 and Figure 7. This is a factor 3-15 faster than that indicated by the e-folding value for the measured reflectivity decay, suggesting that dispersion by wind shears was the main operating mechanism.

To test this, we have run a simple advection model in which the IC is dispersed by the zonal winds and their shears. The model solves the advection equation for a passive tracer under a purelly zonal wind which depends on latitude and height. In this simple approximation no diffusion is incorporated and the only equation to solve is:

$$\frac{\partial q}{\partial t} + u \frac{\partial q}{\partial x} = 0, \qquad (1)$$

where q is the density of the debris material and u is the zonal wind depending on the latitude and height.The numeric code is a straightforward simplification of the two-dimensional code used by Hueso et al. (2002). In this case the model domain consists of a 2500x400 grid points for longitude and latitude and 11 vertically detached layers are computed simultaneously to incorporate effects of a vertical wind shear. The horizontal grid points are separated by 40 km while the vertical layers are representative of close-in levels in the stratosphere. For the zonal wind we impose the parabolic fit to the zonal wind profile shown in Figure 7 in the central layer, with the winds vertically varying from one layer to the next by 1 ms^{-1} faster or slower when above or below the central layer. Therefore the model incorporates a total vertical wind shear of 10 ms^{-1} with each vertical layer decoupled from the rest. We started the simulations by placing a double oval-shaped cloud that mimics the main streak and the halo or crescent area of the observed IC (Sanchez-Lavega et al., 2010), oriented in the longitude-latitude plane as observed (Figure 11) and with the same structure in all 11 vertical layers. The cloud density is uniform within the two areas that compose it but differing in their value from the streak to the halo in a grey scale that represents the observed initial reflectivity. Figure 11 shows snapshots of the simulations with the cloud advected and dispersed by the winds for a time period of 40 days. The simulation produces an evolving debris cloud whose vertically integrated density decreases with an e-folding time of 10 days produced by the combination of both zonal and vertical shears. Stripes in the figure appear from the limited number of vertical layers used which each vertical layer moving with a slightly different zonal wind compared to the others.

Although the zonal expansion and growth of the dense parts resemble those observed for the IC (Figures 1 and 2), there are still differences with what is observed, as for example the failure to reproduce the north-south "horn-shaped" form of the simulated expansion, that is not observed.

[Figure 11]

To explain the differences between the simulated and the observed evolution of the global IC expansion, we must invoke other mechanisms than simply the structure of the zonal winds. Among them are the action of local thermal winds that could have developed from the temperature anomaly originated by the energetic impulse of the impact. From the wind data at this latitude the geostrophic balance can be assumed since the Rossby number $Ro = u / f L \sim$ 0.005 (here u = 10 ms^{-1}, $L \sim$ 7000 km, approximately the westward jet width, and $f = 2\Omega \sin \varphi$ = 2.88x10^{-4} s^{-1}). Orton et al. (2011) measured temperature differences of ~ 3 - 6 K between the impacted area and surroundings a few days after the impact. Assuming that this temperature contrast occurred over the same pressure level, the induced local thermal wind should reach a speed difference between pressure *levels* P_0 *and* P_1 of the order of (Sánchez-Lavega, 2010)

$$|\Delta V| \sim \left(\frac{R_g^*}{f}\right)\left(\frac{\partial T}{\partial x}\right)_P \ln\left(\frac{P_0}{P_1}\right) \qquad (4)$$

Here R_g^* =3740 Jkg^{-1}mol^{-1}K^{-1} and $\partial T / \partial x \sim$ 3-6 K/10,000 km and thus for $\ln(P_0 / P_1) \sim \ln(300/10)$ we have ΔV ~ 12 - 25 ms^{-1}. This value represents probably an upper limit to the induced local thermal winds above background winds that should manifest both zonal and meridional components. Their action could have been added to the ambient regular Jovian winds to disperse the aerosols within the IC. More detailed calculations that consider, for example, the spatial and temporal structure of the spot thermal anomaly are required to try to reproduce the expansion characteristics.

4.2 Clumps (spot) formation within the IC

The high-resolution images of the IC obtained in July and August 2009 showed the formation of clumps or compacted spots with a typical size of ~ 500 – 1000 km within the background of a quasi-homogeneous aerosol field (Figs. 1-2 and 8, Hammel et al., 2010). The spots stand out in the UV by their darkness and in the methane bands by their brightness, indicating they have a higher optical depth (particle density) than the surrounding IC aerosols. The spots were concentrated in the anticyclonic part of the wind profile and their total number was about 14 on August 3. They disappeared in a matter of days probably by mergers between them, whereas others were dispersed by the wind shears, mixing with the background aerosol field.

Their distribution within the IC and their structure suggest that these spots may be vortices resulting from local instabilities. The high resolution HST images (Hammel et al., 2010) do not show well defined spot boundaries, but instead they seem to be elongated with irregular edges and filaments. The ambient flow in the anticyclonic part of the IC has a local vorticity $\zeta = du/dy = -4.2\text{x}10^{-6}$ s^{-1}, about two orders of magnitude lower than the planetary vorticity $f = 2\Omega \sin\varphi = -2.9\text{x}10^{-4}$ s^{-1}. The interaction of the background flow with the spots will produce a small tangential speed at its periphery of the order $V_T \sim \varsigma R/2 =$ 1-2 ms^{-1}, with R its size (effective radius). However, these spots could have other vorticity sources and thus be highly speeding rotating vortices. Unfortunately the HST resolution does not allow us to track features rotating around them.

In order to constrain the action of possible instabilities in generating these clumps we can compare their size with some characteristic dynamical scales that are related to different flow instability mechanisms. For example, one important scale for the formation of baroclinic eddies in quasi-geostrophic (QG) theory of a continuously stratified atmosphere is the first (internal) Rossby deformation radius $L_D = NH/f$ (see e.g. Gill, 1982; Vallis, 2006) where a factor π in the denominator has been omitted, as usually done. This scale has been shown to be important in models of regular Jovian vortices (Shetty et al., 2007; de Pater et al., 2010b and references therein). Here N is the Brunt-Väisälä frequency that in the Jovian stratosphere is $\sim 1.9\text{x}10^{-2}$ s^{-1} and H is usually taken to be the scale height ~ 22 km, which gives L_D ~ 1400 km. Simple scaling will give baroclinic eddy velocities (Vallis, 2006) $v_e \sim (L_e / L_D) < u > \sim$ 4-8 ms^{-1} where we have taken an eddy scale L_e ~ 500 – 1000 km (that of the clumps) and a mean flow velocity $<u>$ ~ 10 ms^{-1}. The corresponding eddy time scale is $\tau_e \sim (L_e / v_e) \sim$ 1 day. Weaker vortices are obtained if, instead of this value for H, we use the vertical extent of the IC, i.e. we assume that the spots extend vertically along the layer occupied by the IC, then $H_{IC} = H \ln$ (300 mbar/1-10 mbar) ~ 3.5-5.5H, L_D ~ 5000 - 8000 km and v_e ~ 0.5 - 1 ms^{-1}.

Since the vertical shear of the zonal flow is low, another important scale to be considered is that associated to the barotropic instability of the westward jet where the IC formed. Ingersoll et al. (1981) showed that Jovian westward jets violate the Rayleigh – Kuo barotropic stability criterion $\beta - d^2u/dy^2 > 0$ being $\beta = df/dy = 2\Omega\cos\varphi / R_p$ the gradient of the Coriolis parameter f (Sanchez-Lavega, 2010). The characteristic horizontal scale associated to this instability is $\sim \pi L_\beta = \pi\sqrt{u/\beta}$ with growing times $\tau_\beta \sim 10/\sqrt{u\beta}$ (Kuo 1949, 1973, see also Stone, 1976). For u ~ 10 ms^{-1} and $\beta = 2.9\text{x}10^{-12}$ ms^{-1} at this latitude we get L_β = 1800 km and τ_β ~ 20 days. The size of the clumps are within the order of magnitude of L_D and L_β . This simple scale analysis indicates that baroclinic or barotropic instabilities could plausibly have played a role in the clump formation.

4.3 Numerical simulations of thermally induced instability in the stratosphere

We have studied the dynamical response of the Jovian atmosphere with the properties of the impact latitude to an instantaneous and localized thermal pulse using the EPIC code ("Explicit Planetary Isentropic-coordinate", Dowling et al., 1998). Our purpose is to see how the potential vorticity (PV) field resulting from an impact and assumed to represent a passive tracer of the flow, mimics the shape, extent, structure and evolution of the IC. Details of EPIC model simulations of the Jovian atmosphere have been extensively described in our previous papers (e,g. Morales-Juberías et al., 2003; García-Melendo et al., 2005; Legarreta and Sánchez-Lavega, 2008; Sánchez-Lavega et al., 2008).

We introduce a localized thermal pulse in an EPIC model atmosphere that tries to simulate the thermal anomaly produced by the impact. We have run series of numerical simulations to draw maps of the evolution of the potential vorticity (PV), selecting two atmospheric levels for the representations, located at ~ 45 and 400 mbar, that corresponds to the IC formation altitudes.

The model atmosphere depends on several free parameters, the most important being the vertical and meridional structure of the zonal wind velocity $U(y,z)$ and the vertical thermal structure represented here by the static stability or Brunt-Väisälä frequency. The three-dimensional structure of the wind field is separated as a product of two functions $U(y,p) = u_h(y)u_v(P)$ where $u_h(y)$ is the wind profile at the cloud tops and $u_v(p)$ is a nondimensional vertical amplitude factor. For the meridional wind profile $u_h(y)$ at cloud-top level we used that derived from HST images in 2007 (Figure 7) locating it at a pressure level $P_0 = 500$ mbar. For the vertical structure we used a two-segment linear dependence in lnP as in García-Melendo et al. (2007). For $P_0 < 500$ mbar we tested winds that slightly decrease, are constant or slightly increase with altitude according to the expression $u_v(P) = 1 + m \ln (P/P_0)$ with an e-folding scale m in steps from +7, 0, -10 scale heights, i.e. winds that change their speed in 1/e in these scale height values. This range covers the observed vertical wind shear at the impact latitude (i. e. a westward jet that increases its eastward speed with altitude) as well as other possibilities to test the sensitivity of the atmospheric response to the vertical shear sign. For $P > 500$ mbar, we assume that the winds remain constant with depth. For the thermal structure, for pressures lower than P_0 we used the thermal profile obtained from radio occultation experiments (Lindal et al., 1981); below cloud tops (pressures greater than P_0), the thermal profile was extrapolated by a wet adiabat characterized by the value of the static stability of the lower levels (see details in García-Melendo et al., 2005; Legarreta and Sánchez-Lavega, 2008; Sánchez-Lavega et al., 2008).

Two groups of simulations were run in a channel that spans latitudes from -38° to -68° using 8 vertical layers: (1) A low-resolution set with a model domain that covers 60° in longitude and with 256 x 128 grid elements in longitude and latitude respectively and (2) A high-resolution set with a model domain that covers 60° in longitude and 15° in latitude with 512 x 128 grid elements In this second set, the spatial resolution was 0.12° per grid element equivalent to 149 km in latitude and 80 km in longitude (the range in longitude for the domain we used is 60 km to 100 km). We performed a total of 160 simulations each of which extended between 25 and 50 days in time. The disturbance produced by the impact was simulated by introducing an instantaneous initial heat source in the EPIC code with a power ranging from 10 to 10,000 Wm^{-2}, and occupying a size of 10° in longitude by 3° in latitude (approximately that of the initial IC, also similar to the temperature anomaly in Orton et al., 2011) and extending vertically from the upper troposphere to the lower stratosphere (pressure range from 1 mbar to 1 bar). We used an hyperviscotity coefficient (Dowling et al., 1998) $\nu^6 =$

0.57x10^{27} m^6s^{-1} that for a scale ΔL = 400 km gives a diffusion time scale $\Delta t_D = (\Delta L)^6 / \nu^6 \simeq 100$ Earth days which is above the length of our simulations.

The results, in the form of the evolution of potential vorticity (PV) maps at the two selected levels (specify levels), show that the most important parameter controlling the PV-field is the impact power. For input powers ~ 500 Wm^{-2} the PV-field evolution follows a pattern that resembles one produced by the passive advection of the IC as discussed in section 4.1. The simulated PV field reproduces the essentials of the IC evolution, i.e. its zonal expansion along the anticyclonic side of the zonal flow. In Figure 12 we show the result of one of the best simulations for which the PV field evolution at the 180-mbar altitude level most closely resembles the observations of the aerosol reflectivity evolution. When higher input powers are introduced (above 500 Wm^{-2}) the PV-field tendency is to form a vortex rotating in anticyclone sense following the ambient wind shear vorticity. The vortex tends to produce wave instabilities and turbulence around it and in the adjacent latitudes (those corresponding to the polar waves discussed in the introduction of section 4), that are not evident in the observations of the cloud and thermal fields. The simulations produce spots of PV within the large vortex, rotating around its centre. One possibility for the clump formation is that they result from the interaction of the IC with pre-existing, underneath to the IC, regular Jovian meteorological features (e. g. vortices and waves). Our EPIC model cannot capture this since these meteorological phenomena were not introduced in the initial simulations.

The potential vorticity field as drawn from the EPIC calculations (Figure 12) shows large values of its gradient at latitudes -52° and -61°. This potential vorticity gradient could have acted as a barrier to the meridional transport of the IC aerosols (see section 3.3), as seen for example in the compound transport in the Earth's stratospheric ozone hole (McIntyre, 1989).

[Figure 12]

4.4 Aerosol optical depth evolution and sedimentation.

In order to reproduce the observed variation of reflectivity in the 2.2-2.3 μm methane absorption band, we used the same vertical structure of the impact debris as was used in previous studies for dates closer to the impact (de Pater et al., 2010a). In that work, the impact site reflectivity was fitted from the ultraviolet to the near infrared with essentially two layers of aerosols. The upper layer contains particles with a mode radius $a = 0.75$ μm, a particle density of 1.2 part/cm^3, and with a vertical range of 10 – 110 mbar; the lower layer has particles with the same mode radius, but a particle density of 5.6 part/cm^3 and distributed in a higher pressure range of 110 – 200 mbar. Since the contribution of the layers below 200 mbar to the observed reflectivity at 2.3 μm is negligible (see contribution functions at Fig.14b from de Pater et al., 2010), we fitted the observed temporal dependence of the reflectivity by varying the particle optical thickness at the only two aerosol layers above this altitude in de Pater et al. (2010) model. The only free parameter in the model was therefore the particle concentration at such layers. We assumed three different scenarios for the density evolution: (A) Particles from both layers were removed simultaneously and at the same rate; (B) the upper particle layer was emptied first, followed by the lower second layer; and (C) the lower layer was emptied first, followed by the upper one. Dynamically, scenario (A) seems more realistic, but scenarios (B) and (C) provide upper and lower limits for the particle concentration retrieval at each layer.

Results are shown in Fig. 13. Both layers have to be drained to explain the observed reflectivity decay (Figure 9), and all three scenarios provide a similar decay law. The second lower layer (which was also initially denser) is about one order magnitude denser at the final stages, with a particle concentration lower than $n_{lower} < 0.5$ part/cm^3, whereas the first upper layer reaches densities not higher than $n_{upper} < 0.03$ part/cm^3. Scenario (B) provides a fast depletion of the upper layer and a much slower depletion of the lower one, just the opposite of what scenario (C) shows.

[Figure 13]

According to this model, the total particle optical thickness decay within the IC can be fitted by an exponential function of the form

$$\tau(t) = 0.014 + \left[0.41 \quad \exp\left(-\frac{(\Delta t - 5046)}{t_D} \right) \right] \qquad (5)$$

where we find $t_D = 14.5$ days, similar to the 15 days that we found from our fit to the observations (eq. 3). This decay law is also similar to that observed in the long-term analysis of the SL9 impact clouds whose evolution was more complex due to the mergers between close but different impact clouds and their subsequent dispersion (Sanchez-Lavega et al., 1998a). For the particle concentration at each layer we get

$$n_{upper}(t) = 0.028 + \left[0.84 \quad \exp\left(-\frac{(\Delta t - 5046)}{t_D} \right) \right] \qquad (6)$$

$$n_{lower}(t) = 0.13 + \left[4 \ \exp\left(-\frac{(\Delta t - 5046)}{t_D} \right) \right] \qquad (7)$$

where time is given in days in the reduced Jovian date scale (section 3.1) and the particle concentration is given in part/cm^3. The exponential decay law is consistent with a horizontal spread of the aerosols by the wind shears as described in Sánchez-Lavega et al. (1998a). Assuming that the total number of particles in a given volume nA remained constant during their transport, the column density n and the area of the site A obey the continuity equation

$$\frac{1}{n}\frac{dn}{dt} = -\frac{1}{A}\frac{dA}{dt} \approx \frac{1}{t_D} \qquad (8)$$

whose solution is equation (6)-(7). A similar relationship can be formulated for the optical thickness $\tau = \pi a^2 QnH$, with Q the scattering efficiency factor, with a solution of the type of equation (5).

Particle sedimentation can also contribute to the evolution of the IC optical depth. We have studied the particle density evolution due solely to sedimentation as in Sánchez-Lavega et al. (1998a). The aerosol sedimentation time depends on the particle size and atmospheric properties that can be characterized by two dimensionless numbers, the Knudsen number (Kn) and the Reynolds number (Re). In the Jovian stratosphere (altitude levels 10-20 mbar) we have $Kn = \ell / a \sim 2$ and $Re = (2\rho a w)/\eta \sim 1.3\text{x}10^{-6}$, with ℓ the gas molecular mean free path, $a = 0.75$ µm the particle radius, ρ the gas density, *w* the vertical fall velocity and η the dynamic viscosity. The values for the latter parameters have been taken from Sánchez-Lavega et al. (1998a). These values bound the dynamical mechanisms that act on the aerosols between those of the laminar and gas kinetic regimes, giving a sedimentation time for the particles $t_S \sim 45 - 200$ days. This suggests that the aerosol sedimentation is only important over long time scales, i.e., removing aerosols via sedimentation well after the IC debris has been dispersed by the winds, thus effectively after November 2009.

5. CONCLUSIONS

The evolution of the IC's debris from the Jupiter impact on 19 July 2009 mimics that seen for the SL9 impacts in 1994, although in 2009 it was easier to determine the evolution as it was generated by a single impact. The structure and long-term evolution of the IC showed that in the stratosphere (up to ~ 1-10 mbar altitude level) and within the latitude band occupied by the IC (from 53.5ºS to 6S1.5º), the zonal motions were still dominant, although they were decreasing their eastward motion.

The westward flow at the impact latitude became weaker with altitude, *i.e.*, it increased its eastward velocity upward above the tropopause. The two bounding north and south eastward jets appeared to be less intense in their velocity peak. Thus globally, the zonal flow became weaker with altitude. This confirms previous studies on the wind vertical structure based on the temperature measurements in the stratosphere and application of the thermal wind relationship (Simon-Miller et al., 2006).

In addition, this study confirms that the meridional motions in the stratosphere were also weak and, at least at this latitude, confined between the two contiguous directionally opposed zonal jets. This is consistent with the thermal-IR analysis (Orton et al., 2011; Fletcher et al., 2010), which also indicates horizontal divergence over the impact latitude. However we note that this is at odds with the SL9 impact debris meridional motions that spread much more in latitude, moving northwards, as showed by Sánchez-Lavega et al. (1998a) and by HCN measurements (Griffith et al., 2004).

The evolution of the IC was mainly produced by the aerosol dispersion by the zonal wind flow, with the particles advected according to the wind shear. However, explaining the details of the IC structure, such as the formation of clumps (condensation spot), is not easy and deserves further study. These clumps may be vortices generated by the wind shear under the action of some kind of dynamical instability. Local motions induced by the temperature anomaly produced by the impact, superimposed to those related to the Jovian background dynamics, could have also contributed to the IC evolution. Because of the Jovian stratospheric properties and small particle size composing the IC, the residence time of the aerosols is large, with sedimentation acting effectively in removing them after several months. This is in agreement with the observations that showed the aerosol particles still present almost 6 months after impact and undetectable 6 months after the impact.

Since we did not detect changes in the system of circumpolar waves located north and south of the impact region we conclude that the dynamical effect of the impact remained confined in latitude. This indicates that the response of the atmosphere to the energy deposited by the impact was merely local, not affecting the dynamics of the closest latitudes.

Acknowledgements

This work was supported by the Spanish MICIIN project AYA2009-10701 with FEDER and Grupos Gobierno Vasco IT-464-07. This research made use of the computing facilities at CESCA in Barcelona with the help of the Ministerio de Educación y Ciencia. The research described in this paper that was performed by Orton and Yanamandra-Fisher was carried out at the Jet Propulsion Laboratory, California Institute of Technology, under a contract with the National Aeronautics and Space Administration. Fletcher was supported by a Glasstone Science Fellowship at the University of Oxford. A. J. Burgasser is a Hellman Fellow. We thank IRTF staff members Schelte ("Bobby") Bus and Tony Denault for their help in creating a command script (macro) that provided minimal interference with the primary programs scheduled on several nights of observation using SpeX. The 1.52m Carlos Sánchez Telescope is operated on the island of Tenerife by the Instituto de Asatrofísica de Canarias in the Spanish Observatorio del Teide. The Hubble Space Telescope data were obtained under GO/DD-12003, GO/DD-12045, and GO-11559 with support provided by NASA through a grant from the Space Telescope Science Institute, which is operated by the Association of Universities for Research in Astronomy, Inc., under NASA Contract NAS 5-26555.

References

Allen, D., Schoeberl, M., Herman J., 1999. Trajectory modeling of aerosol clouds observed by TOMS, *J. Geophys. Res.*, **104**, 27461-27471.

Asay-Davis X.S., M. H. Wong, P.S. Marcus, and I. de Pater, 2011. Changes in Jupiter's Zonal Velocity Profile between 1979 and 2008. *Icarus*, **211,** 1215-1232.

Banfield, D., Gierasch, P.J., Squyres, S.W., Nicholson, P.D., Conrath, B.J., Matthews, K., 1996. 2 μm Spectrophotometry of Jovian Stratospheric Aerosols—Scattering Opacities, Vertical Distributions, and Wind Speeds. *Icarus*, **121**, 389-410.

Barrado-Izagirre, N., Sánchez-Lavega, A., Pérez-Hoyos, S., Hueso, R., 2008. Jupiter's Polar Clouds and Waves from Cassini and HST images: 1993-2006. *Icarus*, **194**, 173-185.

Boville, B. A., Holton, J. R., Mote, P. W., 1991. Simulation of the Pinatubo aerosol cloud in general circulation model. *Geophys. Res. Lett.*, **18**, 2281-2284.

Cano, J. A., 1998. L.A.I.A.: Laboratorio de Análisis de Imágenes Astronómicas. Grup d'Estudis Astronòmics, Barcelona.

Cidadao, A., 2001. Thoughts on super-resolution planetary imaging. *Sky &Telescope* **102**, 127–134.

Clarke, J.T., Prange, R., Ballester, G.E., Trauger, J., Evans, R., Rego, D., Stapelfeldt, K., Ip, W., Gerard, J.C., Hammel, H, 1995. HST far-ultraviolet imaging of Jupiter during the impacts of comet Shoemaker-Levy 9, *Science*, **267**, 1302-1307.

de Pater, I., Fletcher, L.N., Pérez-Hoyos, S., Hammel, H.B., Orton, G.S., Wong M.H., Luszcz-Cook, S., Sánchez-Lavega, A., Boslough, M. 2010a. A Multi-Wavelength Study of the 2009 Impact on Jupiter: Comparison of High Resolution Images from Gemini, Keck and HST. *Icarus*, **210,** 722-741.

de Pater, I, M. H. Wong, P. Marcus, S. Luszcz-Cook, M. Ádámkovics, A. Conrad, X. Asay-Davis, C. Go, 2010b. Persistent rings in and around Jupiter's anticyclones – Observations and theory, *Icarus*, **210,** 742-762.

Dowling, T. E., A. S. Fischer, P. J. Gierasch, J. Harrington, , R. P. Lebeau, and C. M. Santori. 1998. The Explicit Planetary Insentropic-Coordinate (EPIC) Atmospheric Model. *Icarus*, **132**, 221-238.

Fletcher, L.N., Orton, G.S., de Pater, I., Mousis, O., 2010. Jupiter's Stratospheric Hydrocarbons and Temperatures after the July 2009 Impact from VLT Infrared Spectroscopy. *Astron. & Astrophys*, **524**, A46 (doi: 10.1051/0004-6361/201015464).

Grafton, E., 2003. Get ultrasharp planetary images with your CCD camera. *Sky & Telescope* **106**, 125–128

Kuo, H. L., 1949. Dynamical instability of two-dimmensional non-divergent flow in a barotropic atmosphere. *J. Meteorol.,* **6**, 105-122.

Kuo, H. L., 1973. Quasi-geostrophic flows and instability theory. *Adv. Appl. Mathem.,* **13**, 247-330

García-Melendo, E., Sánchez-Lavega, A., Dowling, T., 2005. Jupiter's 24ºN highest speed-jet: Vertical structure deduced from nonlinear simulations of a large-amplitude natural disturbance, *Icarus*, **176,** 272-282.

García-Melendo, E., Legarreta, J., Sánchez-Lavega, A., Hueso, R., Pérez-Hoyos, S., González, J., Gómez-Forrellad J.M. and the IOPW Team, 2009. The Jovian anticyclone BA I. Motions and interaction with the GRS from observations and non-linear simulations. *Icarus*, **203**, 486-498.

Gill, A., 1982. Atmosphere-Ocean Dynamics, Volume 30 (International Geophysics Series), Academic Press Ins, San Diego (California)

Griffith, C. A., Bézard, B., Greathouse, T., Lellouch, E., Lacy, J., Kelly, D., Richter, J., 2004. Meridional transport of HCN from SL9 impacts on Jupiter, *Icarus*, **170**, 58-69.

Hammel, H.B., Beebe, R.F., Ingersoll, A.P., Orton, G.S., Mills, J.R., Simons, A.A., Chodas, P., Clarke, J.T., de Jong, E., Dowling, T.E., 1995. HST Imaging of atmospheric phenomenae created by the impact of comet Shoemaker-Levy 9, *Science,* **267**, 1288-1295.

Hammel, H.B., Wong, M.H., Clarke, J.T., de Pater, I., Fletcher, L.N., Hueso, R., Noll, K., Orton, G.S., Pérez-Hoyos, S., Sánchez-Lavega, A., Simon-Miller, A.A., Yanamandra-Fisher, P.A., 2010. Jupiter after the 2009 Impact: Hubble Space Telescope Imaging of the Impact-generated Debris and its Temporal Evolution. *Astrophys. J. Lett.*, **715,** L150-L154.

Hueso, R., A. Sánchez-Lavega, and T. Guillot (2002), A model for large-scale convective storms in Jupiter, *J. Geophys. Res.*, 107(E10), 5075, doi:10.1029/2001JE001839.

Hueso R., Legarreta, J., Pérez-Hoyos, S., Rojas, J.F., Sánchez-Lavega, A., Morgado, A., 2010. The International Outer Planets Watch Atmospheres Node database of Giant Planets images, *Planet. Space Sci.*, **58,** 1152-1159.

Jónsson, H., Wilson, J., Brock, C., Dye, J., Ferry, G., Chan, K., 1996. Evolution of the stratospheric aerosol in the northern hemisphere following the June 1991 volcanic eruption of Mount Pinatubo: Role of tropospheric-stratospheric exchange and transport, *J. Geophys. Res.*, **101**, 1553-1570.

Karkoschka, E., Tomasko, M. G., 2010. Methane absorption coefficients for the jovian planets from laboratory, Huygens and HST data, *Icarus*, **205,** 674-694.

Lindal, G. F. et al., 1981. The atmosphere of Jupiter: An analysis of the Voyager radio occultation. *J. Geophys. Res.* **86**, 8721–8727.

Legarreta, J., Sánchez-Lavega, A., 2008. Vertical structure of Jupiter's troposphere from nonlinear simulations of long-lived vortices, *Icarus*, **194** 184-201.

McCormick, M. P., Veiga, R. E., 1992. SAGE II measurements of early Pinatubo aerosols, *Geophys. Res. Lett.*, **19**, 155-158.

McIntyre, M. E., 1989. On the Antarctic ozone hole. *J. Atmos. Terr. Phys.*, **51**, 29-43.

Morales-Juberías, R., Sánchez-Lavega, A., Dowling, T., 2003. EPIC simulations of the merger of Jupiter's White Ovals BE and FA: Altitude dependent behavior, *Icarus*, **166**, 63-74.

Orton, G.S., L. N. Fletcher, C. M. Lisse, P. W. Chodas, A. Cheng, P. A. Yanamandra-Fisher, K. H. Baines, B. M. Fisher, A. Wesley, S. Perez-Hoyos, I. de Pater, H. B. Hammel, M. L. Edwards, A. P. Ingersoll, O. Mousis, F. Marchis, W. Golisch, A. Sanchez-Lavega, A. A. Simon-Miller, R. Hueso, T. W. Momary, Z. Greene, N. Reshetnikov, E. Otto, G. Villar, S. Lai and M. Wong 2011.The atmospheric influence, size, and possible asteroidal nature of the July 2009 Jupiter impactor. *Icarus*, **211,** 587-602.

Sánchez-Lavega, A., Lecacheux, J., Colas, F., Gómez, J.M., Laques, P., Miyazaki, I., Parker, D.C., 1995. Motions of the SL9 impact clouds, *Geophys. Res. Lett.*, **22**, 1761 - 1764.

Sánchez Lavega, A., Gómez, J.M., Rojas, J.F., Acarreta, J.R., Lecacheux, J., Colas, F., Hueso, R., Arregui, J., 1998a. Long-term evolution of comet SL-9 impact features: July 1994 – September 1996, *Icarus*, **131**, 341 – 357.

Sánchez Lavega, A., Hueso, R., Acarreta, J.R., 1998b. A system of circumpolar waves in Jupiter's stratosphere, *Geophys. Res. Lett.*, **25**, 4043-4046.

Sánchez-Lavega A., and 24 collaborators, 2008. Depth of a strong jovian jet from a planetary-scale disturbance driven by storms. *Nature*, **451**, 437- 440.

Sánchez-Lavega, A., A. Wesley, G. Orton, R. Hueso, S. Perez-Hoyos, L. N. Fletcher, P. Yanamandra-Fisher, J. Legarreta, I. de Pater, H. Hammel, A. Simon-Miller, J. M. Gomez-Forrellad, J. L. Ortiz, E. García-Melendo, R. C. Puetter, 2010. The impact of a large object with Jupiter in July 2009. *Astrophys. J. Lett.*, **715** L155-L159.

Sánchez-Lavega, A. 2010. *An Introduction to Planetary Atmospheres*, 587 pp., Taylor & Francis, CRC Press (Boca Raton, Florida).

Shetty, S., Xylar S. Asay-Davis, P. S. Marcus, 2007. On the Interaction of Jupiter's Great Red Spot and Zonal Jet Streams. *J. Atmos. Sci.*, **64**, 4432–4444.

Simon, A., and Beebe, R.F., 1996. Jovian Tropospheric Features—Wind Field, Morphology, and Motion of Long-Lived Systems. *Icarus,* **121**, 319-330.

Simon-Miller, A., Conrath, B.J., Gierasch, P.J., Orton, G.S., Achterberg, R.K., Flasar, F.M., Fisher, B.M., 2006. Jupiter's atmospheric temperatures: From Voyager IRIS to CIRS, *Icarus*, **180**, 98-112.

Stone, 1976. Jupiter's Atmospheric Dynamics, in *Jupiter,* T. Gehrels ed., University of Arizona (Tucson, AZ).

Stowe, L. L., Carey, R. M., Pellegrino P. P., 1992. Monitoring the Mt. Pinatubo aerosol layer with NOAA/11 AVHRR data, *Geophys. Res. Lett.*, **19**, 159-162.

Trepte, C., Veiga, R., McCormick, M., 1993. The Poleward Dispersal of Mount Pinatubo Volcanic Aerosol, *J. Geophys. Res.*, **98**, 18563-18573.

Vallis, G. K., 2006. Atmospheric and Oceanic Fluid Dynamics. Cambridge University Press, 745 pp. (Cambridge, U. K.)

Vincent, M . B. and 18 colleagues, 2000. Jupiter's Polar Regions in the Ultraviolet as Imaged by HST/WFPC2: Auroral-Aligned Features and Zonal Motions, *Icarus,* **143**, 205-222.

West, R.A., Karkoschka, E., Friedson, A.J., Seymour, M., Baines, K.H., Hammel, H.B., 1995. Impact debris particles in Jupiter's stratosphere, *Science*, **267,** 1296-1301.

TABLE 1. Observatories contributing with images to this study

Observatory	***Telescope (diameter) & Instrument (*)***	***Wavelengths***	***Date coverage Month (days)***
IOPW network (1)	(1)	350 – 950 nm	Jul (21,22,23,24,25,26,27,29,30,31), Aug(1,2,3,4,5,6,7,8,9,10,11,12,13,14,15,17, 19,20, 22,24,26,27,29,30), Sep (1,5,6,8,10,11,13,15,17,18,20)
HST (2)	WFC3	234 – 924 nm	Jul (23), Aug (3, 8), Sept (22, 23)
Calar Alto (3)	3.5 m – Omega 2000	1.6-2.17 μm	Jul (20,22)
ESO–VLT (4)	8 m - NACO	1.6-2.48μm	Jul(26)
TNG (5)	3.6 m - AdOpt	1-2.3μm	Jul(27), Aug (3,4,13)
WHT (6)	4.2 m - Ingrid	1-2.3μm	Aug (4,5)
Keck (7)	10 m – NIRC2	1.6-2.12 μm	Jul (20, 24, 25), Sep. (7,10)
IRTF–NASA (8)	3 m - SpeX	2.12-2.23 μm	Jul (20,24,26) Aug (2,4,13,14,15,16,18,19,23,25,30) Sep (2,7,8,9,14,20,23,25,30) Oct (1,19,20,25,27,29) Nov (44,8,18,22,23,24,25) Dec (4,5,29,30,31) May (14, 28) [2010]
TCS (9)	1.5 m – CAIN3	1-2.3μm	Oct (7, 23)

Notes:

(*) Telescope diameter and instrument/detector employed. Details for the instrumentation can be obtained in the websites of the Observatories. Other details given in de Pater et al. (2010) and Orton et al. (2011).

(1) IOPW (http://www.ehu.es/iopw) and database PVOL (http://www.pvol.ehu.es/). See Hueso et al. (2010).

(2) Hubble Space Telescope. See details of the observations in Hammel et al. (2010).

(3) Calar Alto Observatory, Centro Astronómico-Hispano Alemán (Almería, Spain)

(4) European Southern Observatory – Very Large Telescope (Chile)

(5) Telescopio Nazionale Galileo (Canary I., Spain)

(6) William Herschel Telescope - ING (Canary I., Spain)

(7) W. M. Keck Observatory (Hawaii, USA)

(8) Infrared Telescope Facility-NASA (Hawaii, USA)

(9) Telescopio Carlos Sánchez (Canary I., Spain)

FIGURE CAPTIONS

Figure 1. Series of cylindrical map projections showing the evolution of the impact cloud (IC) from July 19 to September 23, 2009, in the visible continuum wavelengths ~ 400-650 nm where it appears as a dark feature against the background Jupiter clouds. Dates indicated.

Figure 2. Series of cylindrical map projections showing the evolution of the impact cloud (IC) from July 20 to October 29, 2009, in the near infrared spectral range covering the wavelengths of the methane absorption bands at 890 nm and 2.12-2.3 µm where it appears as a bright feature. Dates are indicated in each panel.

Figure 3. Zonal expansion in System III longitude of the east and west edges (extremes) of the impact cloud (IC), main spot and crescent. Circles: measurements in the near infrared (2.12-2.3 µm) from July 19 to October 29, 2009; Crosses: measurements in the visual range using IOPW and HST images from19 July to 20 September 2009.

Figure 4. Longitudinal drift of individual features within the IC tracked in the visual range from IOPW images. A linear least-square fit to the motion of each feature is shown. Solid black circles correspond to a reference white spot (identified as W Spot placed at latitude -51.05°) not pertaining to IC that showed an oscillation in its longitude motion.

Figure 5. Longitudinal drift of individual features within the IC tracked in the near infrared (2.12-2.3 μm). A linear least-square fit to their motion is shown for each feature.

Figure 6. Latitudinal drift from latitude -56.0° to -53.5° of a single cloud element within the IC, from July 23 to August 5. The inset shows the IC and the arrow marks the direction of the meridional motion of the cloud element.

Figure 7. Left: Zonal wind speeds of each individual element (dots) tracked within the IC using the images obtained in the visual range from IOPW (red) and HST (black), and in the near infrared (blue). Comparison is made with the background zonal wind profile measured in 2007 using the HST images (solid black line with error bars) and with individual features (circles) tracked in the same HST images as the IC. The impact point is represented by a large green circle. Right: All the IC individual cloud motions (dots) and their fit to a simple parabolic wind profile function (red curve) compared with the HST 2007 profile (continuous line).

Figure 8. The east and west expansion of the IC and clump formation in its interior from July 23 to Aug. 3 as observed in the methane absorption bands that sense the IC top aerosol level. The formation and tracking of different spots within IC are marked by the lines and arrows. From top to bottom: July 23 (HST, 890 nm), July 25 (Keck, 2.12 μm), July 27 (TNG, 2.3 μm), August 3 (TNG, 2.3 μm), August 3 (HST, 890 nm).

Figure 9. Long-term evolution of the IC surface reflectivity in the near infrared methane absorption band at 2.2-2.3 μm (crosses) showing the exponential decay fitted

function (solid line). The rectangle marks the reference calibration (see text) and the horizontal line marks the cloud background reflectivity.

Figure 10. Polar map projections of the south polar region of Jupiter from HST images in the ultraviolet (A, B, C) and methane absorption band (D, E, F) showing the impact (dark in UV, bright in the methane band) and the planetary waves at north and south. Dates and wavelengths: (A) July 23, 275 nm; (B) August 3, 225 nm; (C) August 8, 275 nm; (D) July 23, 890 nm; (E) August 3, 890 nm; (F) August 8, 890 nm.

Figure 11. Snapshots of the temporal evolution of the IC after 40 days resulting from a simulation of the IC spread by a purely advection model using 11 vertically detached layers. Each panel shows the vertically integrated amount of debris material with a color code that maximizes the structure. The last panel shows material which is 10 times less bright than the first one. Stripes in this figure appear from the limited number of vertical layers used to represent the vertical wind shear.

Figure 12. Comparison between EPIC numerical simulations and HST observations of the IC. Left: maps of the potential vorticity (PV) at the altitude level corresponding to the 180 mbar isobaric surface in the Jovian atmosphere resulting after 15 and 25 days following an initial impulse thermal anomaly disturbance of 500 Wm^{-2}. Right: HST images of the aerosol impact cloud after 15.1 and 20.5.days from the impact (see also Figure 1).

Figure 13. (a) Total particle optical thickness from 10 mbar to 200 mbar as a function of time. Solid line is used for scenario A and dashed lines for scenarios B (upper line) and C (bottom line). (b) Particle density versus time for upper layer (n_{upper}) and bottom layer (n_{lower}). As in (a), solid line shows scenario A. Note that scenario B yields the bottom dashed line for $\mathrm{n_{upper}}$ and the upper one for n_{lower}, just the opposite to scenario C. See text for more details.

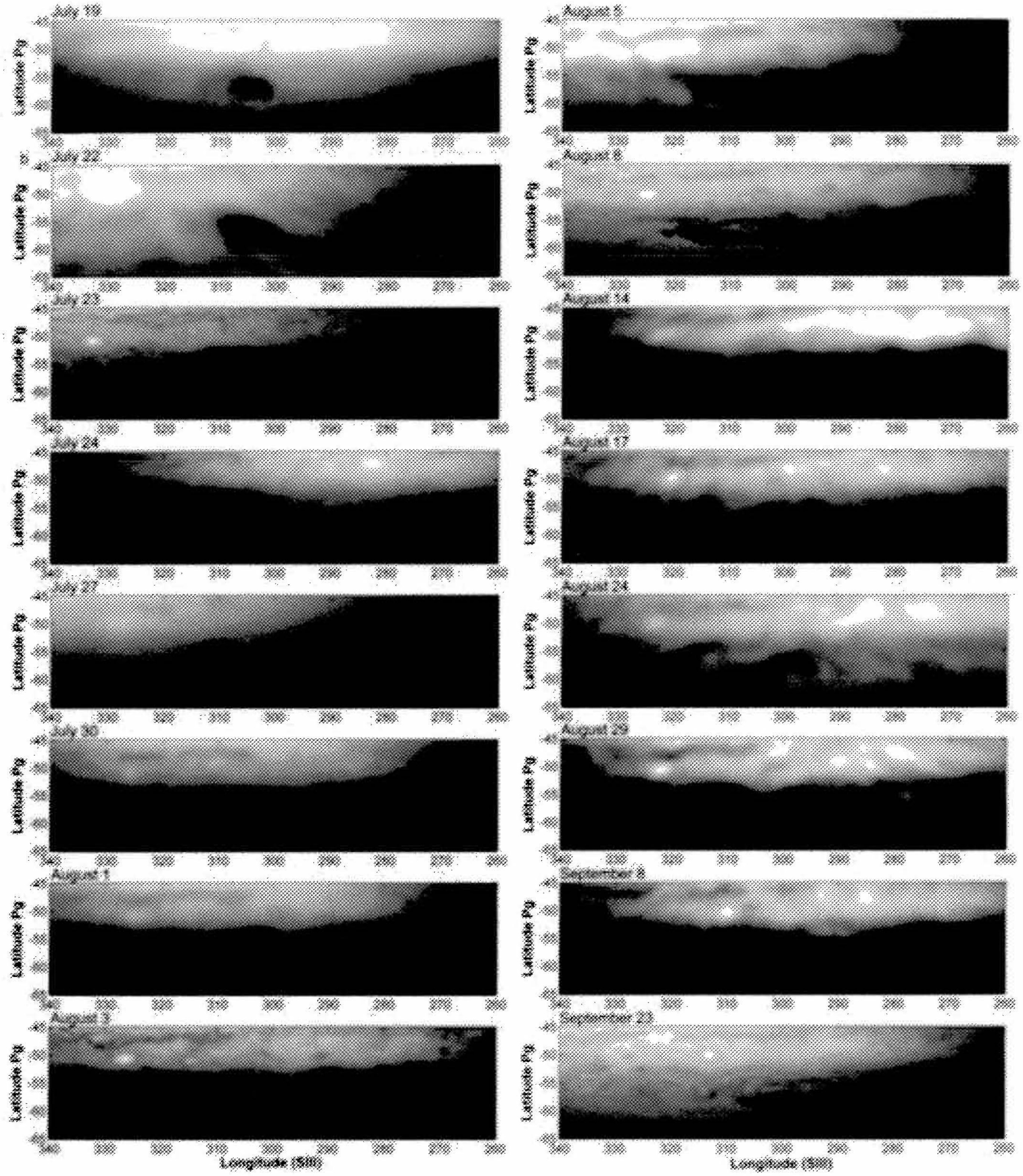
July 19
July 22
July 23
July 24
July 27
July 30
August 1
August 3
August 5
August 8
August 14
August 17
August 24
August 29
September 8
September 23
Latitude Pg
Longitude (SIII)

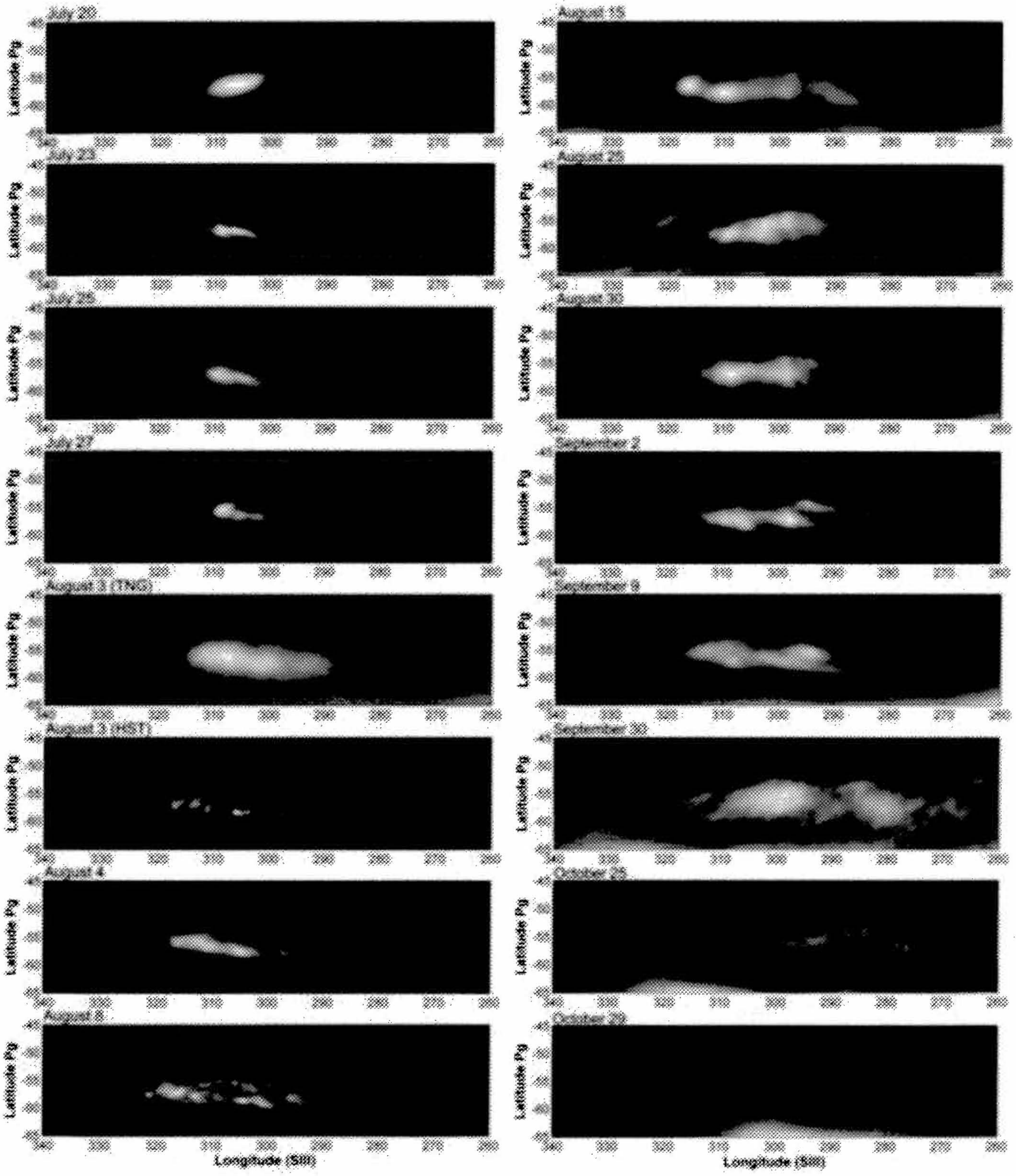
July 20
July 23
July 25
July 27
August 3 (TNG)
August 3 (HST)
August 4
August 8
August 15
August 25
August 30
September 2
September 8
September 30
October 25
October 29
Latitude Pg
Longitude (SIII)
340
330
320
310
300
290
280
270
260

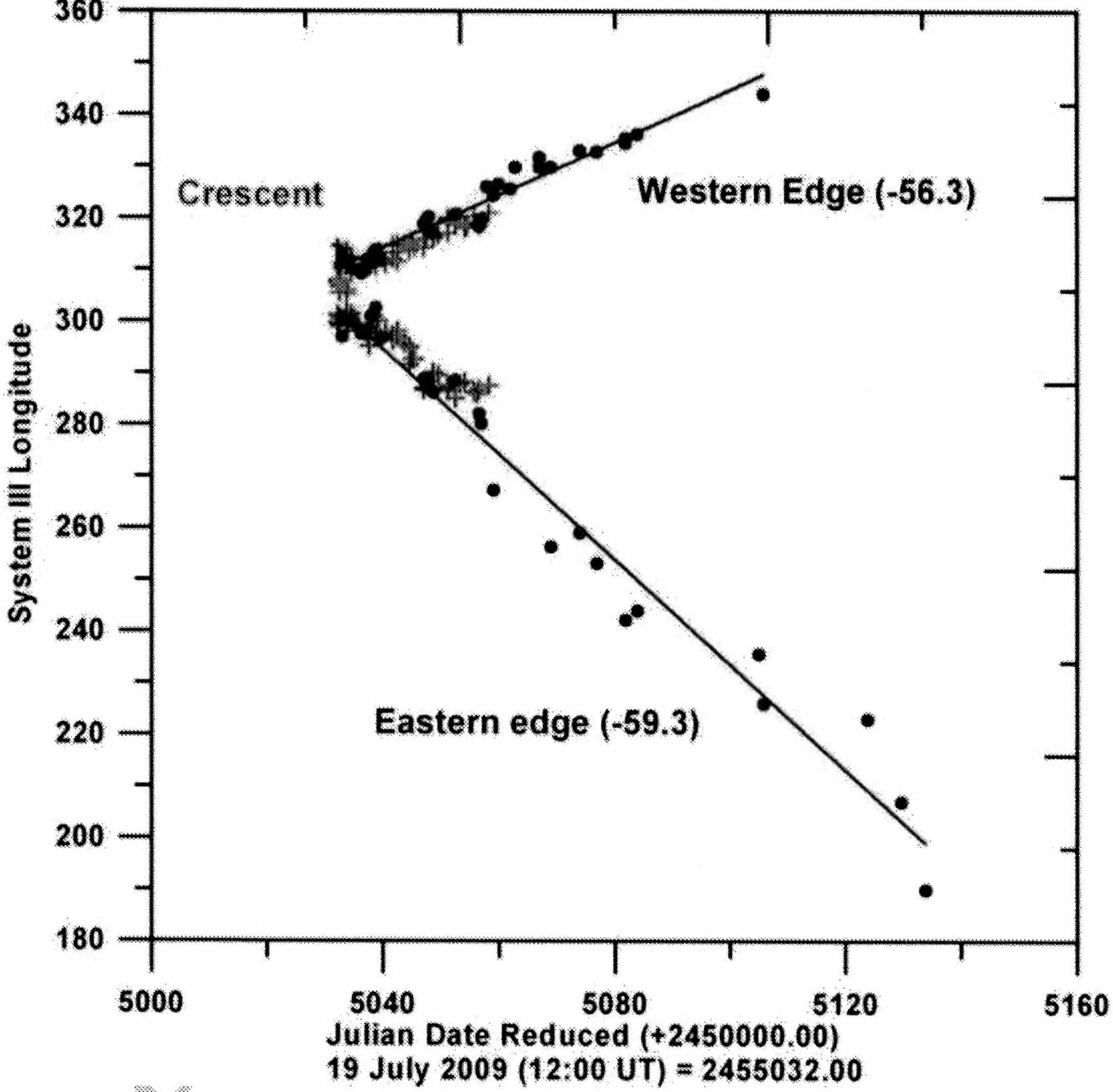
360
340
320
300
280
260
240
220
200
180
System III Longitude
Crescent
Western Edge (-56.3)
Eastern edge (-59.3)
5000
5040
5080
5120
5160
Julian Date Reduced (+2450000.00)
19 July 2009 (12:00 UT) = 2455032.00

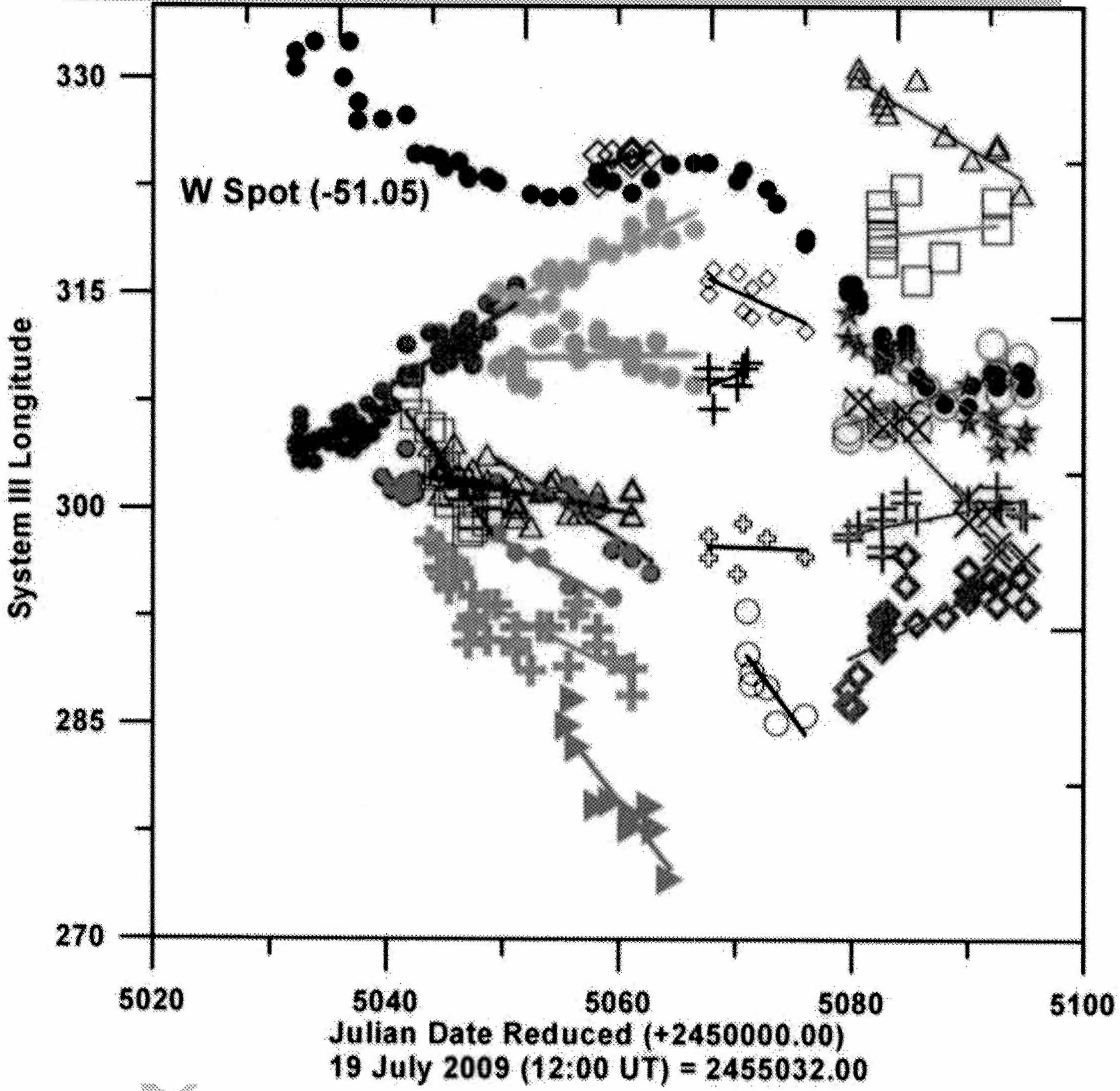
W Spot (-51.05)
System III Longitude
330
315
300
285
270
5020
5040
5060
5080
5100
Julian Date Reduced (+2450000.00)
19 July 2009 (12:00 UT) = 2455032.00

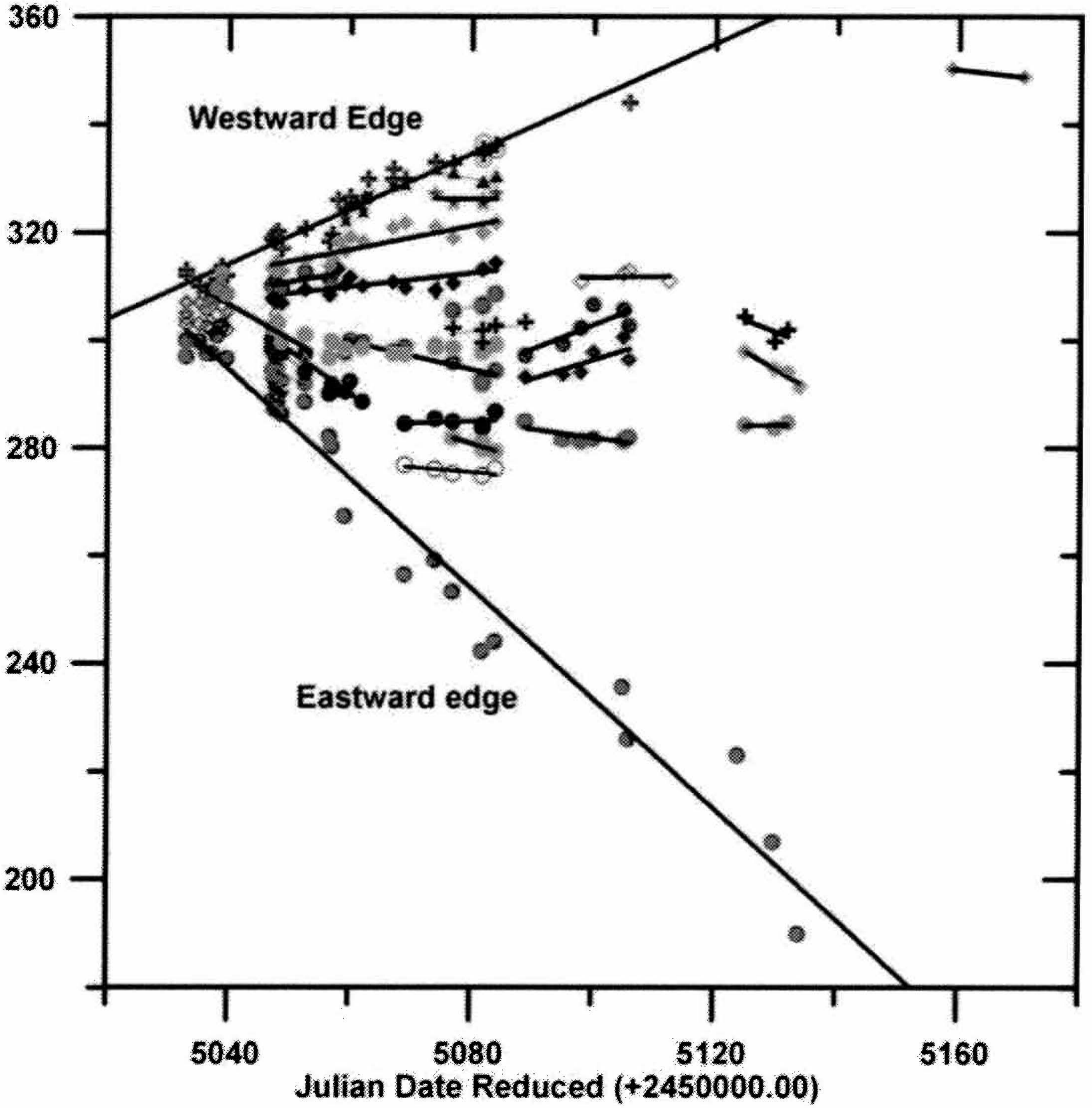
Westward Edge
Eastward edge
360
320
280
240
200
5040
5080
5120
5160
Julian Date Reduced (+2450000.00)

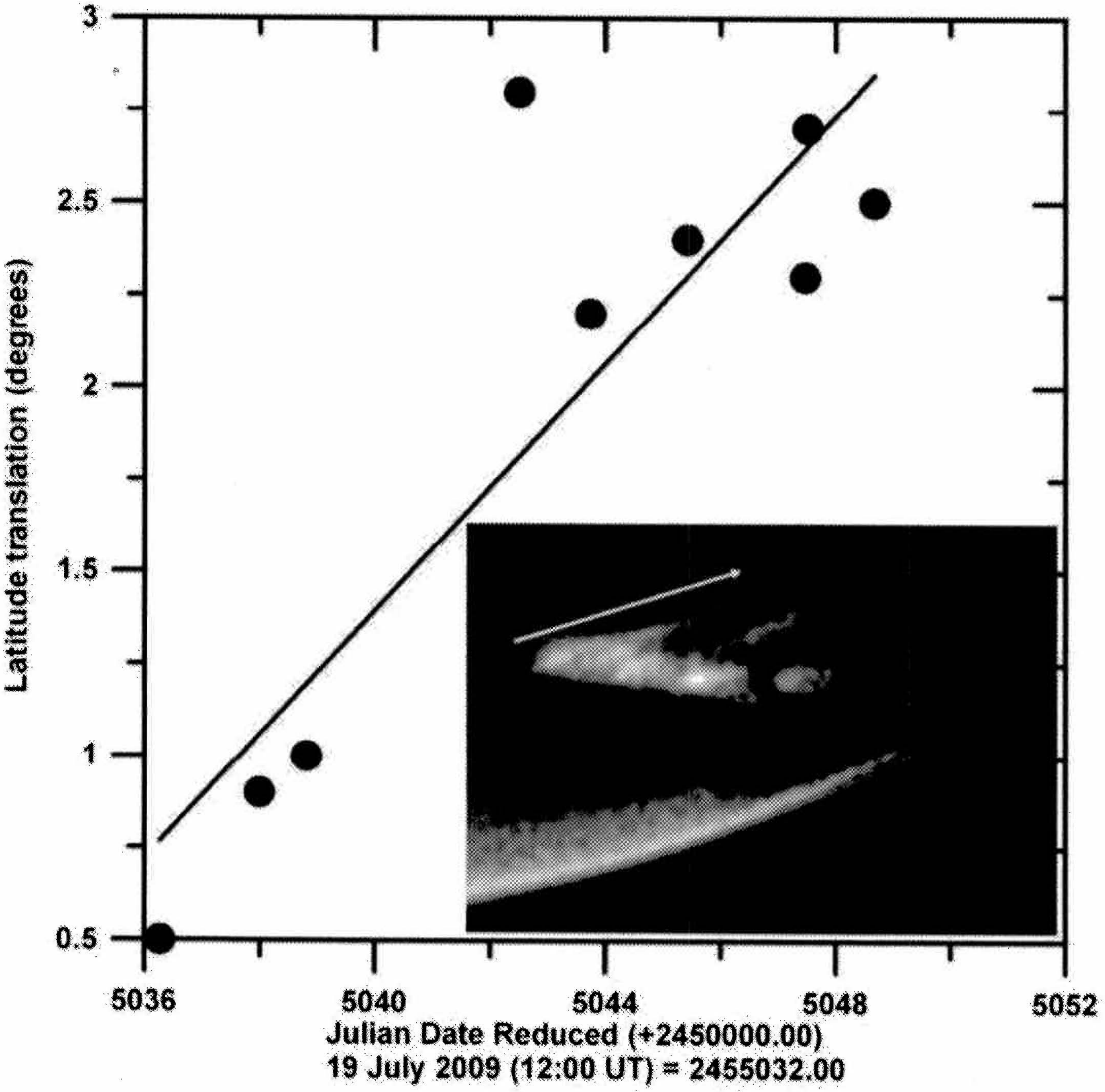
Latitude translation (degrees)
3
2.5
2
1.5
1
0.5
5036
5040
5044
5048
5052
Julian Date Reduced (+2450000.00)
19 July 2009 (12:00 UT) = 2455032.00

AC

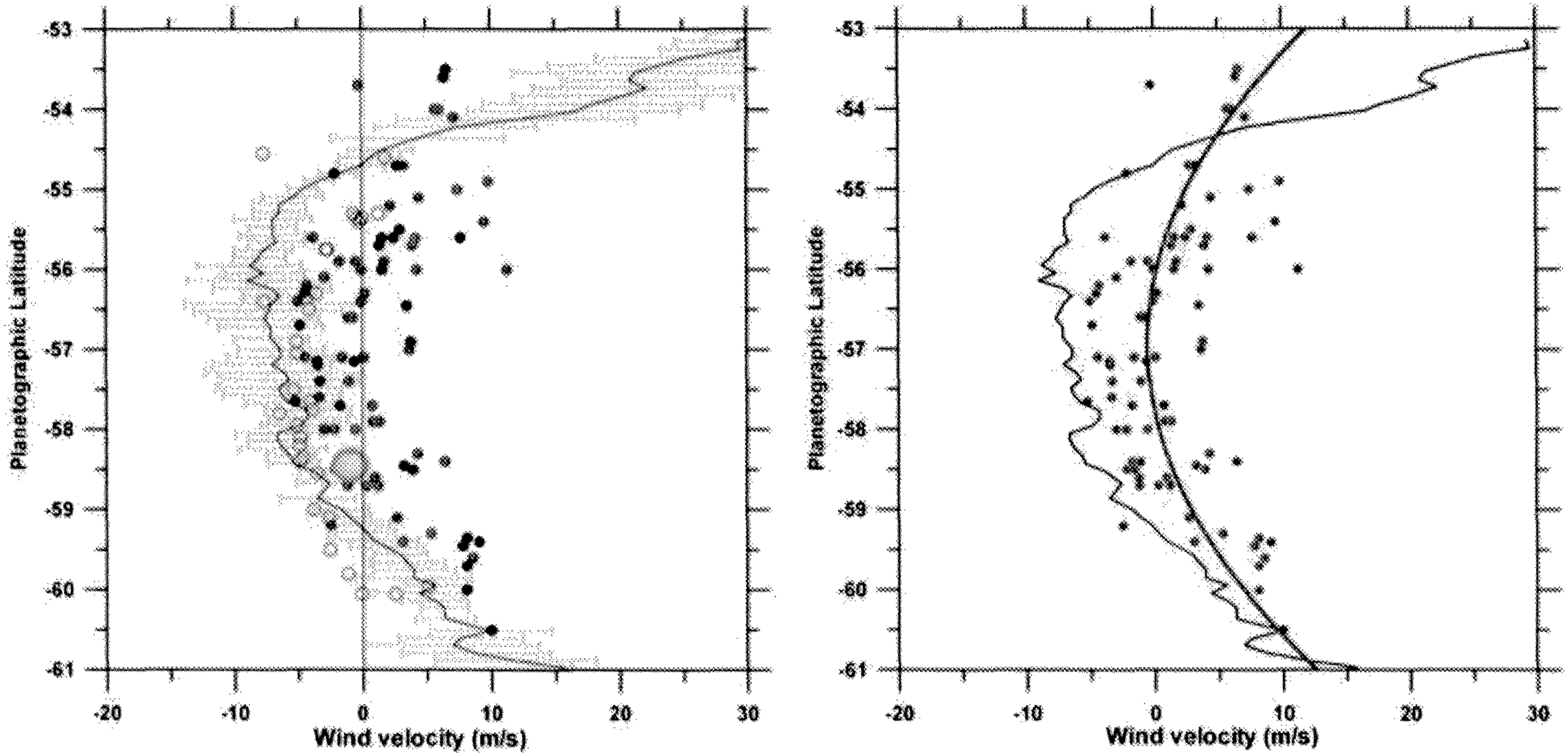
Planetographic Latitude
-53
-54
-55
-56
-57
-58
-59
-60
-61
-20
-10
0
10
20
30
Wind velocity (m/s)
Planetographic Latitude
-53
-54
-55
-56
-57
-58
-59
-60
-61
-20
-10
0
10
20
30
Wind velocity (m/s)

ACCEP

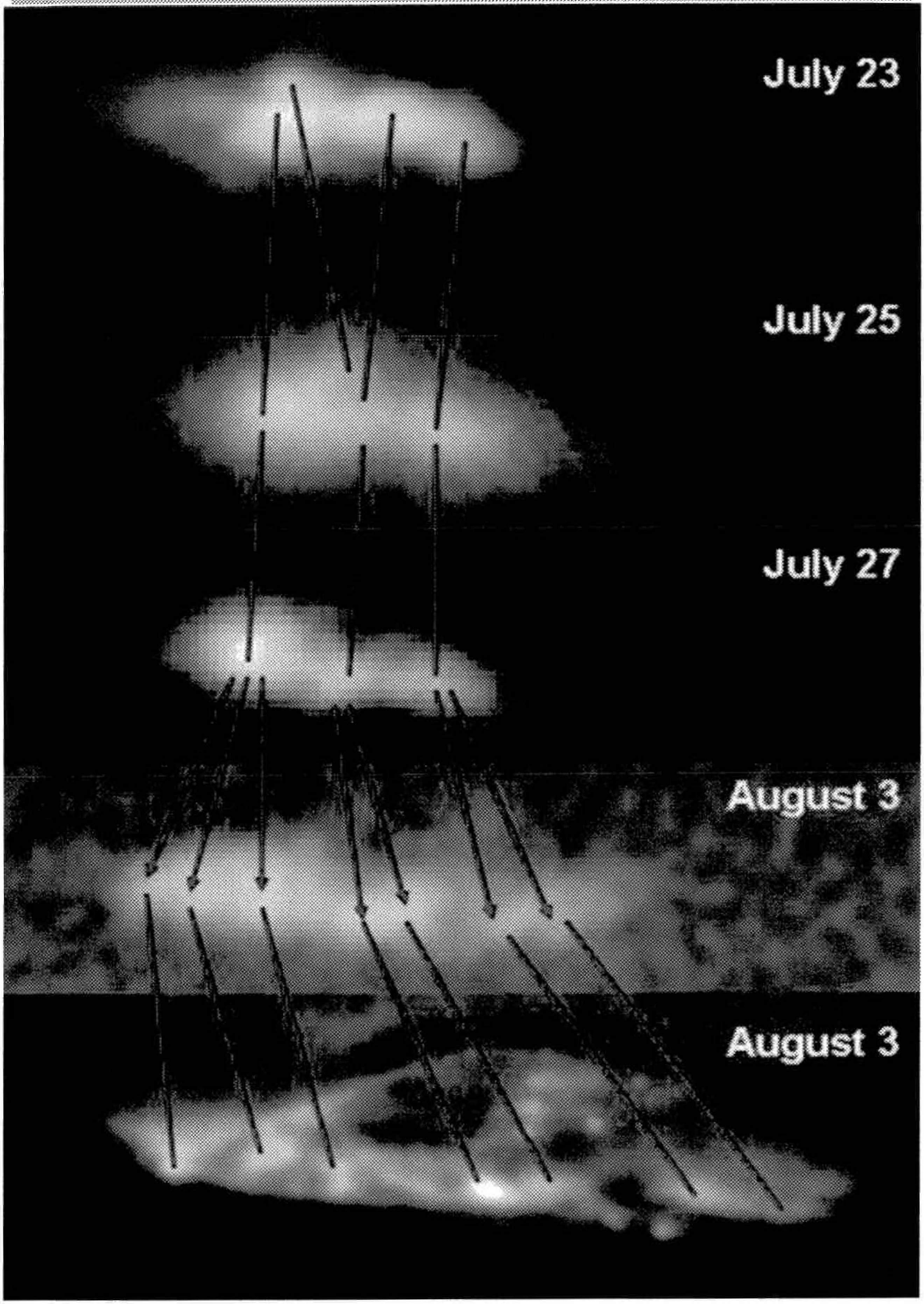
July 23
July 25
July 27
August 3
August 3

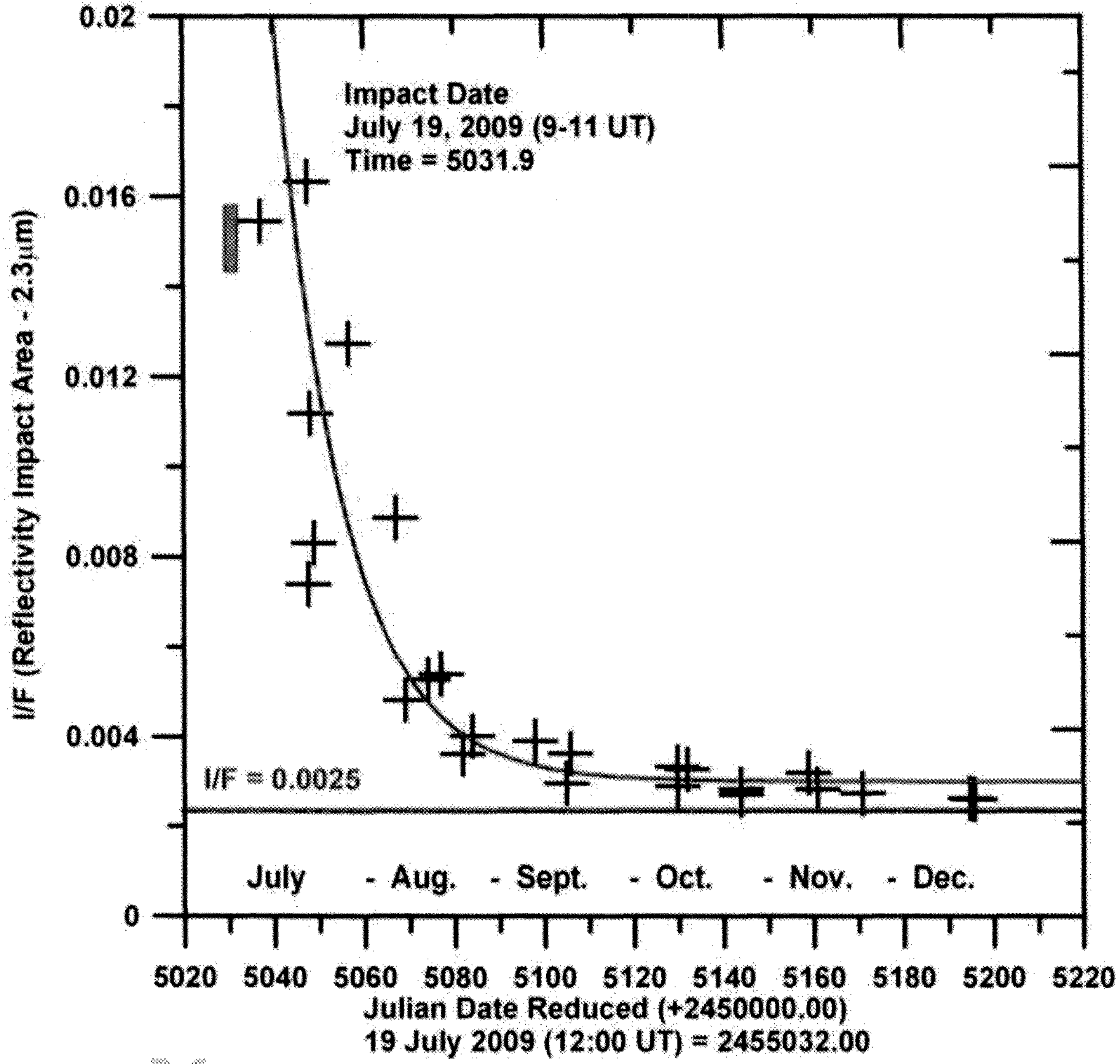
Impact Date
July 19, 2009 (9-11 UT)
Time = 5031.9
I/F = 0.0025
July - Aug. - Sept. - Oct. - Nov. - Dec.
I/F (Reflectivity Impact Area - 2.3μm)
0
0.004
0.008
0.012
0.016
0.02
5020
5040
5060
5080
5100
5120
5140
5160
5180
5200
5220
Julian Date Reduced (+2450000.00)
19 July 2009 (12:00 UT) = 2455032.00

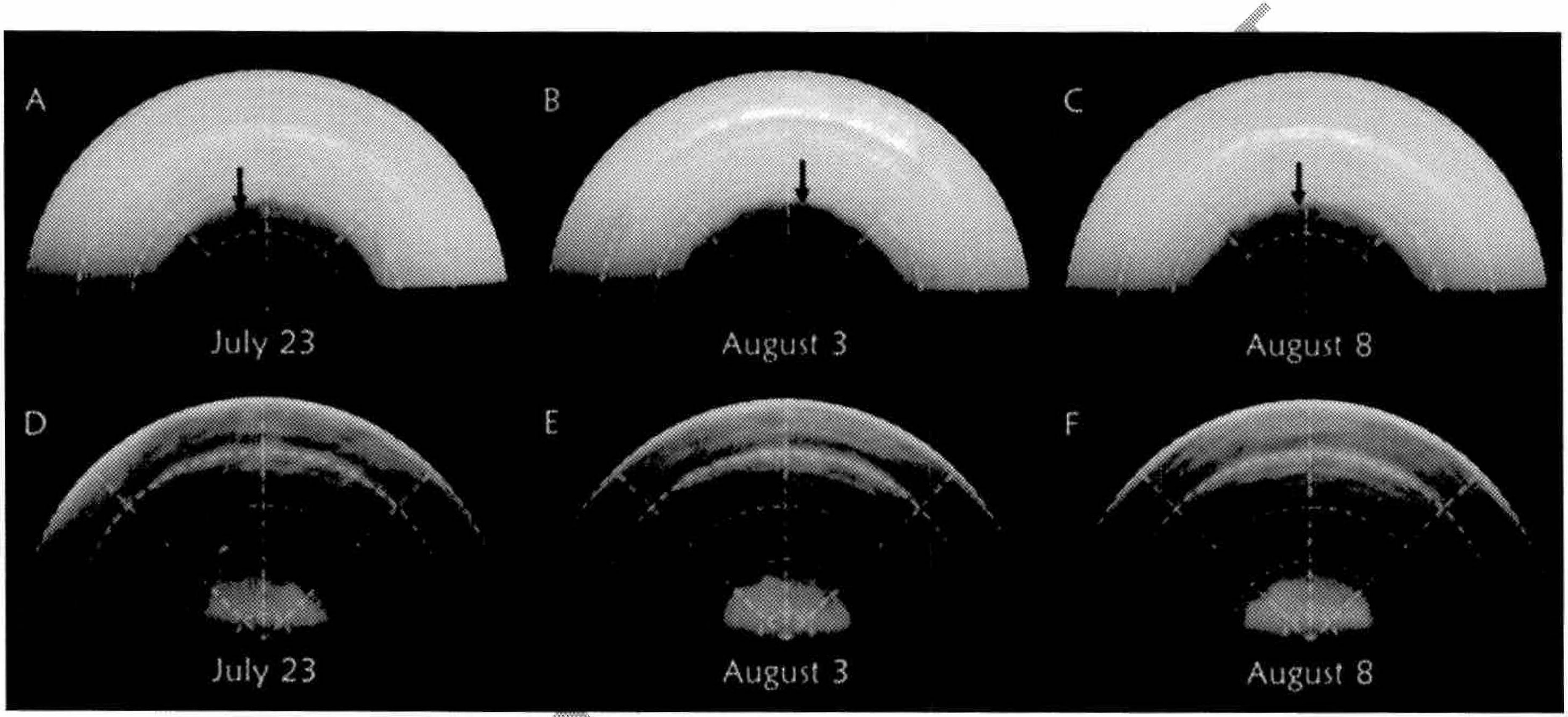
A
B
C
July 23
August 3
August 8
D
E
F
July 23
August 3
August 8

ACCEPT

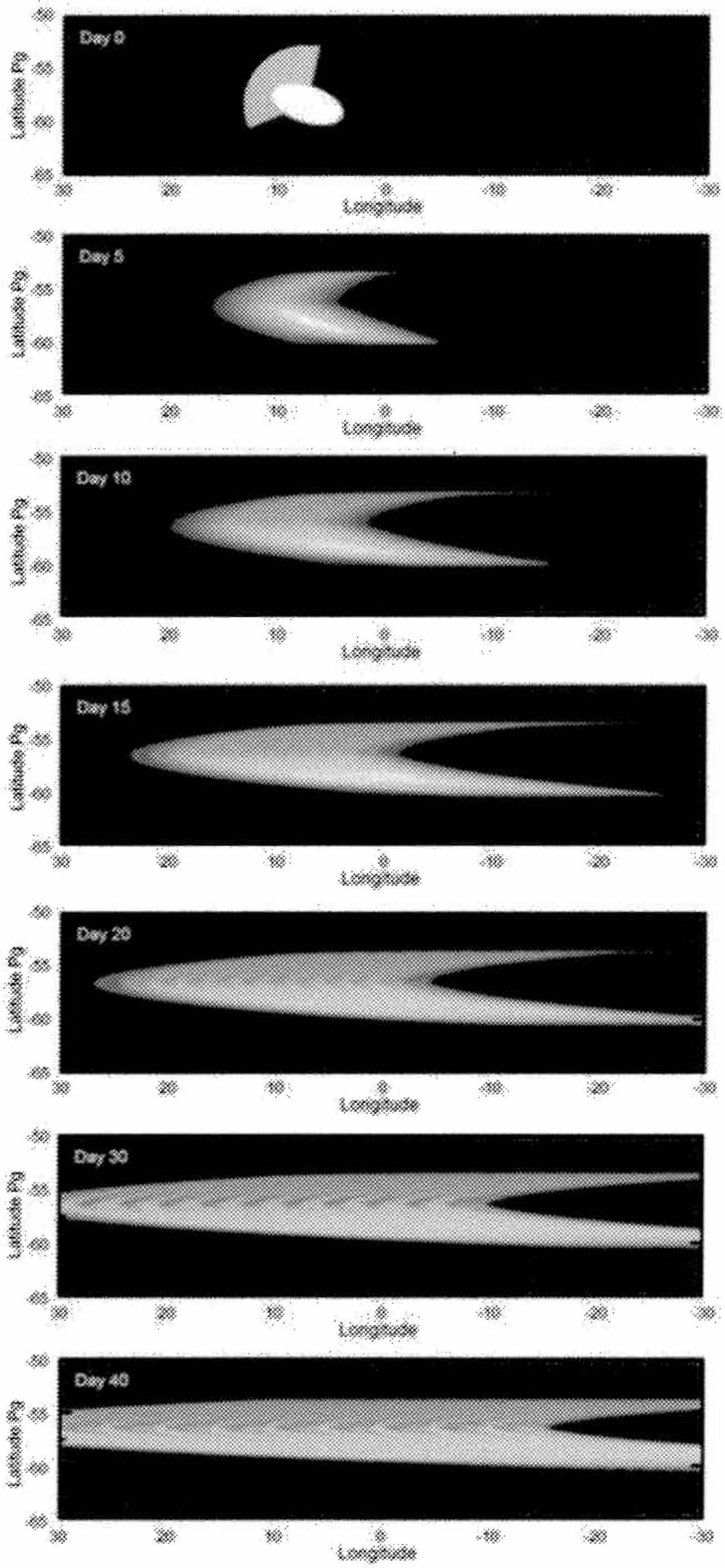
Day 0
Day 5
Day 10
Day 15
Day 20
Day 30
Day 40
Latitude Pg
-50
-55
-60
-65
Longitude
30
20
10
0
-10
-20
-30

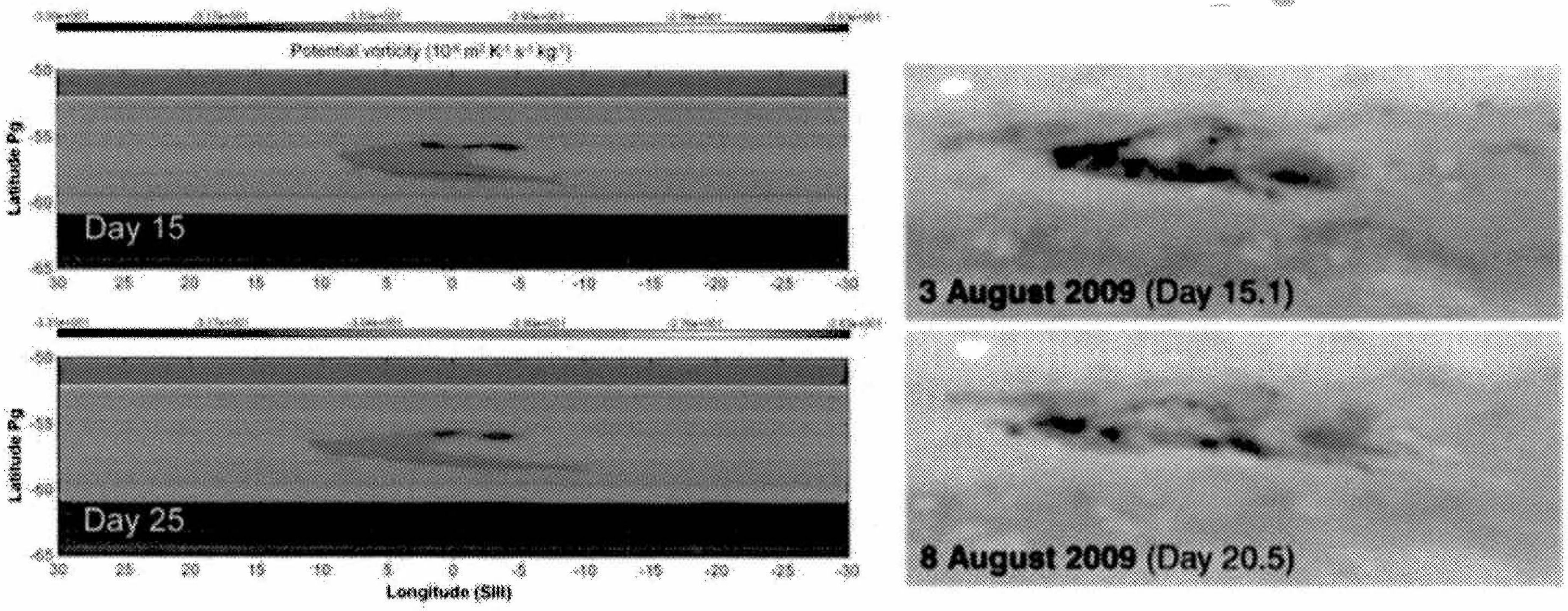
Potential vorticity (10^-6 m^2 K^1 s^-1 kg^-1)
Latitude Pg
-50
-55
-60
-65
Day 15
Day 25
30
25
20
15
10
5
0
-5
-10
-15
-20
-25
-30
Longitude (SIII)
3 August 2009 (Day 15.1)
8 August 2009 (Day 20.5)

ACCEPTED

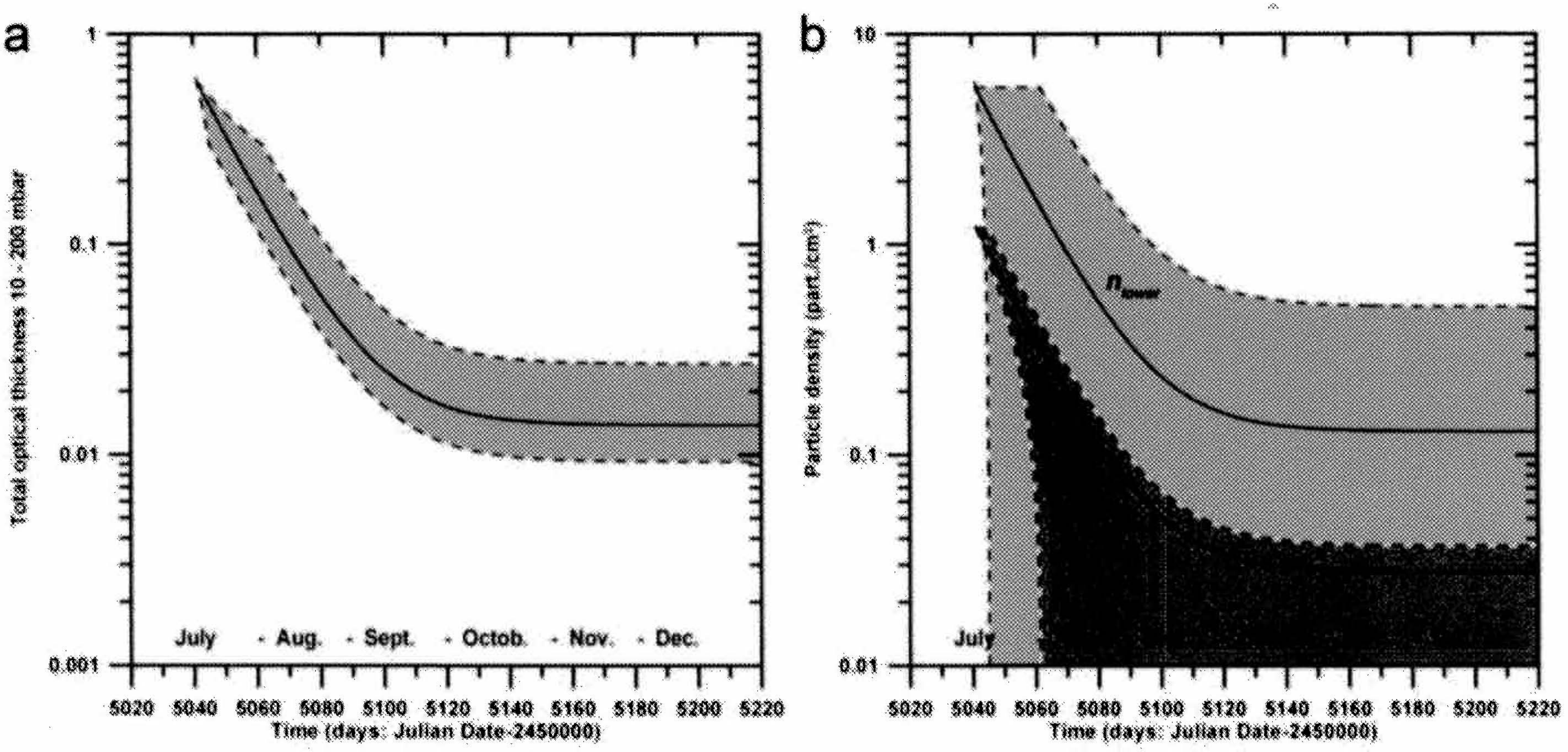
a
Total optical thickness 10 - 200 mbar
1
0.1
0.01
0.001
July
Aug.
Sept.
Octob.
Nov.
Dec.
5020 5040 5060 5080 5100 5120 5140 5160 5180 5200 5220
Time (days: Julian Date-2450000)
b
Particle density (part./cm³)
10
1
0.1
0.01
n_{lower}
July
5020 5040 5060 5080 5100 5120 5140 5160 5180 5200 5220
Time (days: Julian Date-2450000)

ACCEP

We present a study of the long-term evolution of the cloud of aerosols produced in the atmosphere of Jupiter by the impact of an object on 19 July 2009.

The impact cloud expanded zonally from ~ 5000 km to 225,000 km (29 October), remaining meridionally localized within a latitude band from 53.5°S to 61.5°S planetographic latitude.

We find that the westward jet at 56.5°S latitude increases its eastward velocity with altitude with vertical wind shear of 1 ms^{-1} per scale height above the tropopause.

A pure advection of the aerosols by the winds and their shears and a nonlinear simulation (EPIC code) of the evolution of the potential vorticity field generated by a heat pulse, reproduce the observed global structure of the cloud, its optical depth decrease, and the dominant zonal dispersion of the aerosols.